



LUNDS
UNIVERSITET

**Spectral broadening of 4 mJ
femtosecond pulses using a bulk
multi-pass cell**

Master Thesis

by Saga Westerberg

Supervisor: Cord Arnold

Deputy Supervisor: Anne-Lise Viotti

Examineer: Lars Rippe

Division of Atomic Physics
LRAP: 589
Lund University
Lund, Sweden
June 2023

Ultrakorta laserpulser - via olinjär optik!

Ultrakorta laserpulser är bara några femtosekunder (10^{-15} s) långa. De är alltså över på några miljondels miljardels sekunder. Många användningsområden kräver ännu kortare pulser. Det kan röra sig om materialmodifiering på nanoskalan, ögonoperationer, datalagring, eller mätning av händelseförlopp som är över på bara några femtosekunder - eller mindre!

Det finns olika tekniker för att ta en laserpuls och förkorta den i tiden. Teknikerna begränsas av pulsernas intensiteten, vilken måste vara tillräckligt hög för att ljuset ska bete sig olinjärt. Samtidigt måste den vara tillräckligt låg för att inte förstöra materialet som används. I många applikationer behövs dock en så hög intensitet som möjligt så ju mer intensiva pulser som kan komprimeras, desto bättre.

En vanlig enkel laserpekare lyser hela tiden. Den består av en enda våglängd och har ganska låg intensitet. För att kunna skapa pulser behövs fler våglängder som samverkar - de släcker då ut varandra ibland och förstärker varandra ibland. När de förstärker varandra skapas en puls och när de släcker ut varandra skapas ett uppehåll. Ju fler våglängder som finns, desto kortare blir pulsen. Om du då har en puls med 3 våglängder så kommer den att ha en viss pulslängd. Det enda sättet att göra den kortare är genom att lägga till kortare och längre våglängder. Men, hur ska det gå till?

I alla material finns det negativt laddade partiklar - elektroner. När ljus träffar en elektron så kommer den att uppleva det elektriska fältet hos ljuset. En laddad partikel i ett elektriskt fält får en skjuts av det elektriska fältet - ungefär som om du håller i en gunga och drar den fram och tillbaka. Om du gungar gungan försiktigt kommer den bara följa med din rörelse, men om du börjar gunga mer våldsamt så kommer gungan att gunga mer våldsamt den också. Samma sak händer med elektronen, och när gungningen blir våldsam så gör det att nya våglängder sänds ut av elektronen. De nya våglängderna tillsammans med den första kan sedan tryckas ihop i tiden och ge en kortare puls! Hur många nya våglängder vi får ut beror också på hur långt vi går igenom materialet, och då kan också andra önskade effekter uppstå.

För att göra detta i praktiken kan två likadana speglar och en tunn glasskiva användas. En puls får studsas mellan speglarna, och igenom glasskivan. Spegelarna fungerar som linser, och fokuserar ljuset in i glasskivan så att intensiteten blir tillräckligt hög. Men från inledningen så vet du att intensiteten kan bli för hög också! Då förstörs materialet och därmed även pulsen. Ändå går det att göra för en högintensiv laser. Istället för att sätta glaset i fokus kan glasskivan placeras en bit framför fokus - där intensiteten är tillräcklig, men ändå inte för hög.

I mitt projekt har jag använt en laser med så hög intensitet att om den fokuseras joniseras luften - vilket förstör pulsen. Därför har jag istället för två likadana speglar använt en negativt fokuserande spegel - som placerades framför fokus. Med en sådan uppställning möjliggörs ultrakorta pulser med ännu högre intensitet!

Abstract

Nonlinear optical effects can be used for spectral broadening, which is the basis of the field of post-compression of laser pulses. When the intensity of light becomes high enough the refractive index becomes intensity dependent, and as the intensity often varies both with position and time so does the refractive index. The consequence of the position dependence is self focusing, an often unfavorable nonlinear effect, while the time dependence is what enables spectral broadening via self phase modulation (SPM). In this work a novel approach building on nonlinear Multi-Pass Cells (MPC), with the aim of broadening the spectrum of high energy pulses (4mJ) with a short pulse duration (25fs), is designed, implemented and characterized, both spatially and temporally. The obtained spectral broadening is from 50nm to 80nm, and the output beam is astigmatic. In parallel a numerical tool is implemented to study how self focusing affects the spatial beam profile in an MPC. The tool is based on the split step Fourier method for solving the time independent nonlinear Schrödinger equation. To further be able to study realistic beams a tool to apply aberrations via Zernike polynomials is adapted. Results of the simulations show the importance of nonlinear mode matching for high power beams.

Abstract

Olinjära optiska effekter kan användas för spektral breddning, vilket är grunden för post-kompression av laser pulser. Vid tillräckligt höga intensiteter blir brytningsindex intensitets beroende, och då intensiteten beror av både tid och position gör även brytningsindex det. Konsekvensen av positions beroendet är själv-fokusering (self-focusing) en ofta oönskad olinjär effekt. Tidsberoendet möjliggör istället spektral breddning via self phase modulation (SPM), "egen fas modulering". I det här arbetet har ett nytt tillvägagångssätt, baserat på olinjära Multi-Pass celler(MPC) med målet att bredda spektrat av högenergetiska (4mJ) pulser med kort tidsduration (25 fs), designats, implementerats och karakteriserats både spatiellt och temporalt. Spektrat har breddats från 50 nm till 80 nm och den utgående strålen är astigmatisk. Parallellt har ett numeriskt verktyg implementerats för att studera hur self-focusing påverkar pulsens spatiella egenskaper i en MPC. Verktöget är baserat på split stepl Fourier method, och löser den tidsberoende olinjära Schrödinger ekvationen i rummet. För att ytterligare studera realistiska intensitetsprofiler implementerades ett verktyg för att applicera aberrationer genom Zernike polynom. Resultaten av simuleringarna visar vikten av att utnyttja olinjär modmatching då lasern har hög energi.

Acknowledgements

First of all, I would like to thank my supervisors Cord and Anne-Lise. Your guidance and investment within this project is something I have appreciated greatly. Thank you for always believing in me, for all the support and constructive feedback. In addition to improving this work you have also improved my experience.

During this work I have also had the pleasure of working and interacting with a number of wonderful people. Sizou and Mattias, thank you for the hours spent in the lab with me. Thank you Chen for your help on the numerically heavy part of this project, as well as fixing the laser when it gave up. Thank you Anka, Daniel and Ivan for helping me with the FROG and D-scan, both setup and retrieval.

Though I have not mentioned most of you by name, I want to thank all of you working in the atto-group and at the division of atomic physics. You contribute to a working environment where it is pleasant to work, spend time and explore various topics of discussion.

Finally, I would like to thank friends and family. Though you are far away you have always supported me, and though lasers and optics is maybe not your cup of tea, you have not once complained when I have been talking your ears off.

Contents

1	Introduction	1
1.1	Objective	1
1.2	Thesis outline	2
2	Theory	3
2.1	The propagation of light	3
2.2	Gaussian beam	7
2.3	Ultrafast Optics	11
2.4	Nonlinear Optics	13
	2.4.1 Self Focusing	14
	2.4.2 Self Phase Modulation	16
2.5	Multi-Pass cell	18
	2.5.1 Resonator Optics	18
	2.5.2 Multi-Pass cells for Post compression	19
	2.5.3 The Herriott Configuration	19
	2.5.4 Nonlinear phase	21
	2.5.5 Convex Concave MPC	21
3	Designing the MPC	23
3.1	Designing the MPC resonator	23
4	The Experimental Set Up	28
4.1	The Laser Source	28
4.2	Building the MPC	28
4.3	Characterization of the Convex-Concave MPC	30
5	Simulations	35
5.1	Fourier Propagator	35
5.2	Solving the Nonlinear Schrödinger Equation	36
	5.2.1 Verification of the NLSE-SSFM	37
	5.2.2 Simulating the MPC	38
5.3	Realistic Beams	44
6	Conclusion and outlook	52

Chapter 1

Introduction

In 2016 the multi-pass cell (MPC) for spectral broadening technique was demonstrated for the first time [1]. Since then it has been proven a successful post compression technique. It covers a large number of pulse energies and peak powers. The technique is today limited by optical damage, gas ionization and spatio-spectral beam inhomogeneity. Because of this it has been hard to realize with the Ti:Sapphire laser, which has a high peak power and pulse energy, and it has been especially hard to implement in a compact way [2].

Normally MPC's are realized in a Herriott configuration, where two Concave mirrors form a cavity in which the beam is refocused multiple times to obtain Self Phase Modulation, a nonlinear effect that depends on the intensity of light, leading to spectral broadening. For lasers with a high peak Power such as a Ti:Sapphire laser the focus in the middle of the cell would lead to a plasma forming in the air, ruining the pulse's temporal and spatial profile. Recently, a different configuration has been suggested, making a cavity of one concave and one convex mirror [3, 4]. In such a configuration a virtual focus is created, and the plasma formation can be avoided. This would allow for the use of an MPC to achieve spectral broadening while maintaining the beam quality and pulse energy.

The idea of this work is to achieve spectral broadening of a Ti:Sapphire amplifier at 800 nm by using an MPC configuration, utilizing such convex concave mirror setup.

1.1 Objective

The goal of this project is to spectrally broaden the pulses of a titanium sapphire laser, such as the one in the kilo hertz lab at the Division of Atomic Physics in Lund. Applications in the laboratory would benefit from a larger spectral bandwidth. In this project it will be investigated if a multi-pass cell can be used to broaden the bandwidth from 70 nm to 140 nm.

The conventional MPC setup resembles a symmetric cavity with two focusing mirrors between which the beam propagates. This leads to focusing, which for pulses with high energy causes the air in the focus to ionize, causing plasma generation. This is unfavorable in regards of pulse quality and power, and therefore needs to be avoided. Recently a scheme avoiding focusing has been realized for post compression of Ytterbium lasers [3, 4]. One focusing mirror is replaced by a defocusing mirror, and thus the focus is avoided.

One reason for the success of the MPC is its ability to preserve and sometimes even improve spatial beam quality, compared to other applications such as hollow core fibers or multi-plate solutions. Why this is the case is not yet understood, and therefore simulations on the spatial evolution of a beam in an MPC could bring insight on what it is that gives the MPC its desirable properties.

The objective of this project is to i) design and implement multi-pass cell avoiding a focus, ii) characterize the setup in terms of beam quality, transmitted power and spectral broadening and iii) simulate the spatial behaviour of the modes in an MPC as they undergo self focusing.

1.2 Thesis outline

The focus will first be on the theory. Multi-Pass cells (MPC) and nonlinear optics are the main interests, but to properly understand them some theory of Gaussian beams and pulsed light is required.

The process of designing the MPC is presented in chapter 3. The performed calculations are presented along with a comparison to previous work [3, 4]. As a final reality check a ray tracing simulation in FRED is presented and the design choices are discussed.

Next, Chapter 4 describes the experimental set up. First the laser parameters are described, then the MPC set up along with the characterization measurements, and finally the results are presented.

Chapter 5 describes the written simulation code, the tests performed to verify its correctness and some early results.

The final chapter of the thesis contains a conclusion, a short summary and an outlook for future questions and applications.

Chapter 2

Theory

The content of this thesis is based on what was done in form of calculations, simulations, measurements and analysis during the course of this project. The following section is written to provide the reader with the necessary theory to understand what has been done, and with the aim to facilitate further reading. To a large extent it is based on textbooks in optics, such as *Fundamentals of Photonics* by B.E.A. Saleh and M.C. Teich [5], *Principles of Optics* by Born and Wolf [6], *Nonlinear Optics* by R. W. Boyd [7] and *Introduction to Fourier Optics* by J. W. Goodman [8].

First the propagation of light is presented along with the paraxial wave equation. From there, the Gaussian beam is formulated and its formalism presented. This is required to understand optical resonators, necessary for the design process of the MPC. Next the topic of pulsed light is introduced, to understand compression of optical pulses and the time dependent nonlinear effect leading to spectral broadening, Self Phase Modulation (SPM). After this, the nonlinear effects needed for the simulations, self focusing, and to understand the spectral broadening, SPM, are introduced. Finally an overview of MPC's is provided.

2.1 The propagation of light

Propagation of light is, like all waves, described by the wave equation

$$\nabla^2 u + \frac{1}{c} \frac{\partial^2 u}{\partial t^2} = 0 \quad (2.1)$$

where c is the velocity with which the light propagates. In vacuum $c = c_0$ where c_0 is the speed of light $3 \times 10^8 \text{ m s}^{-1}$. On the other hand the speed of light in a material is reduced, as a consequence of the refractive index, n of the material. This relationship $c = c_0/n$ is a consequence of the electric permittivity of the material, which is often linear, though later in this work conditions where it is nonlinear will be treated (see nonlinear optics). If the propagation occurs in a medium, the parameters need to be altered due to the impact of the refractive index;

$$c = \frac{c_0}{n}, \quad \lambda = \frac{\lambda_0}{n}, \quad k = nk_0. \quad (2.2)$$

$$(2.3)$$

The sub-scripted '0' denotes vacuum value.

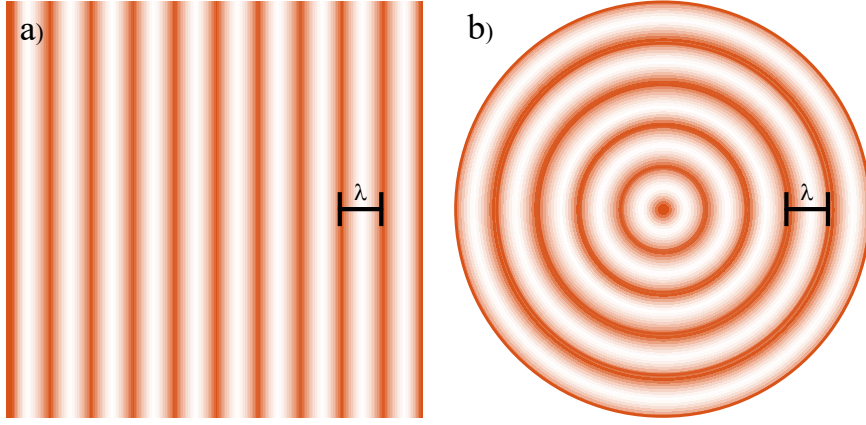


Figure 2.1: Wavefronts of a) planar wave and b) spherical wave. The wavefronts are separated by the wavelength λ .

The Plane Wave

The simplest solution to equation 2.1 is the plane wave

$$u(\mathbf{r}, t) = a(\mathbf{r}) \cos(\omega t + \phi(\mathbf{r})) \quad (2.4)$$

with amplitude $a(\mathbf{r})$, phase $\phi(\mathbf{r})$ and angular frequency ω . The solution is equally represented in complex writing of a plane wave

$$U(\mathbf{r}) = A \exp(-j\mathbf{k} \cdot \mathbf{r}) \quad (2.5)$$

where \mathbf{k} is the wavevector, $U(\mathbf{r})$ is the complex amplitude and A is the complex envelope of the wave. The complex representation is a solution to the Helmholtz equation,

$$\nabla^2 U + k^2 U = 0 \quad (2.6)$$

which can be obtained by Fourier Transforming Eq(2.1). The wavenumber $k = \frac{\omega}{c} = \frac{2\pi\nu}{c}$ is the amplitude of the wavevector \mathbf{k} . Note the dependency on c which implies that k changes depending on the media in which it propagates [6].

The planar wave is monochromatic and infinite in space and time. It is called planar because the wavefronts, which are surfaces of constant phase, are planes perpendicular to the wavevector. The wavefronts are separated in space by the wavelength λ , illustrated in figure 2.1 a), and as time changes the wavefronts move in the direction of \mathbf{k} with the speed c . Any wave can be decomposed into planar wave components, which is the basis of Fourier optics [8].

The Spherical Wave

Another solution to the wave equation is the spherical wave, illustrated in figure 2.1 b),

$$U(\mathbf{r}) = \frac{A_0}{|\mathbf{r} - \mathbf{r}_0|} \exp(-jk|\mathbf{r} - \mathbf{r}_0|) \quad (2.7)$$

which has spherical wavefronts (instead of planar) centered around \mathbf{r}_0 . When the sign of the exponential is negative, as in the equation above, the wavefronts travel

away from the origin \mathbf{r}_0 but, if it is positive the wavefronts instead travel towards \mathbf{r}_0 . An important aspect of the spherical wave is that it may be approximated as a paraboloidal wave, if only a small segment of the wavefront is considered. This holds within the small angle approximation, which is the basis of paraxial rays [5].

Paraxial Waves

When working in the regime of ray optics a convenient simplification is the small angle approximation. This is to say that the ray(s) of interest deviate from the z-axis only by a small angle, allowing said angle to be approximated as $\theta \approx \sin(\theta)$. The same approximation can be applied for waves, but instead it is the wavevector \mathbf{k} that forms a small angle with the z-axis. The wavenumber is the amplitude of the wavevector, $k = |\mathbf{k}| = \sqrt{k_x^2 + k_y^2 + k_z^2}$, and $k_x = \sin(\theta_x)k \approx \theta_x k$ (analogously for y) for a sufficiently small angle θ_x . This can also be used in the Helmholtz equation 2.6 to obtain the *Paraxial Helmholtz equation* using $k_\perp \ll k$.

$$\nabla^2 U + k^2 U = 0 \quad (2.8)$$

$$\nabla_\perp^2 U + \frac{\partial^2 U}{\partial z^2} + k^2 U = 0 \quad (2.9)$$

$$\text{Applying the spatial Fourier Transform } U(x, y, z) \xrightarrow{\mathcal{F}} \mathcal{U}(k_x, k_y, z) \quad (2.10)$$

$$-(k_x^2 + k_y^2)\mathcal{U} + \frac{\partial^2 \mathcal{U}}{\partial z^2} + k^2 \mathcal{U} = 0. \quad (2.11)$$

By introducing operator notation as in [9]

$$P^2 = \frac{\partial^2}{\partial z^2}, \quad Q^2 = k^2 - k_\perp^2 \quad (2.12)$$

$$(2.13)$$

and inserting this in the Fourier transformed Helmholtz equation

$$P^2 \mathcal{U} + Q^2 \mathcal{U} = 0 \quad (2.14)$$

$$(P + iQ)(P - iQ)\mathcal{U} = 0 \Rightarrow P = \pm iQ \quad (2.15)$$

$$P = iQ = i(\sqrt{(k^2 - k_\perp^2)}). \quad (2.16)$$

$$(2.17)$$

This previous step is of great importance, as it determines the direction of propagation. To be able to handle the rest of the derivation only one of the possible solutions to P can be considered, and is the same as selecting a direction of propagation. The wavefronts propagate in the direction of the \mathbf{k} , and the wave equation describes propagation for both \mathbf{k} and $-\mathbf{k}$. Since a selection is performed, the paraxial Helmholtz equation instead describes propagation in only one direction. Continuing with the selected direction of propagation (which can analogously be done for the

other direction)

$$\frac{\partial}{\partial z} \mathcal{U} = -i(\sqrt{k^2 - k_{\perp}^2}) \mathcal{U} = -ik \left(\sqrt{1 - \frac{k_{\perp}^2}{k^2}} \right) \mathcal{U} \quad (2.18)$$

$$\approx -ik \left(1 - \frac{k_{\perp}^2}{2k^2} \right) \mathcal{U} \quad \text{assuming } k_{\perp}^2 \ll k^2 \quad (2.19)$$

$$\Rightarrow 2k \frac{\partial}{\partial z} \mathcal{U} + 2ik \mathcal{U} - ik_{\perp}^2 \mathcal{U} = 0 \xrightarrow{\mathcal{F}^{-1}} \quad (2.20)$$

$$2k \frac{\partial}{\partial z} U - 2ikU + i\nabla_{\perp}^2 U = 0. \quad (2.21)$$

$$(2.22)$$

To continue, the complex envelope $U(\mathbf{r}, z)$ is represented as a plane wave propagating along z (carrier wave), $\exp(-jkz)$ under the influence of an envelope, $A(\mathbf{r})$. Inserting this into the Helmholtz equation,

$$U(\mathbf{r}, z) = A(\mathbf{r}) \exp(-jkz), \quad \frac{\partial}{\partial z} U = \frac{\partial}{\partial z} A \exp(-jkz) - jkA \exp(-jkz), \quad (2.23)$$

$$2k \frac{\partial}{\partial z} A - 2ik^2 A + 2ikA + i\nabla_{\perp}^2 U = 0 \quad (2.24)$$

$$-2ik \frac{\partial}{\partial z} A + \nabla_{\perp}^2 A = 0 \quad (2.25)$$

which is the paraxial Helmholtz equation. Its simplest solution is a paraboloidal wave,

$$A = \frac{A_1}{z} \exp(-jk \frac{(x^2 + y^2)}{2z}) \quad (2.26)$$

which is an approximation of a sphere at small angles, as illustrated in figure 2.2. Another solution of importance is the Gaussian Beam, treated in the next section [5].

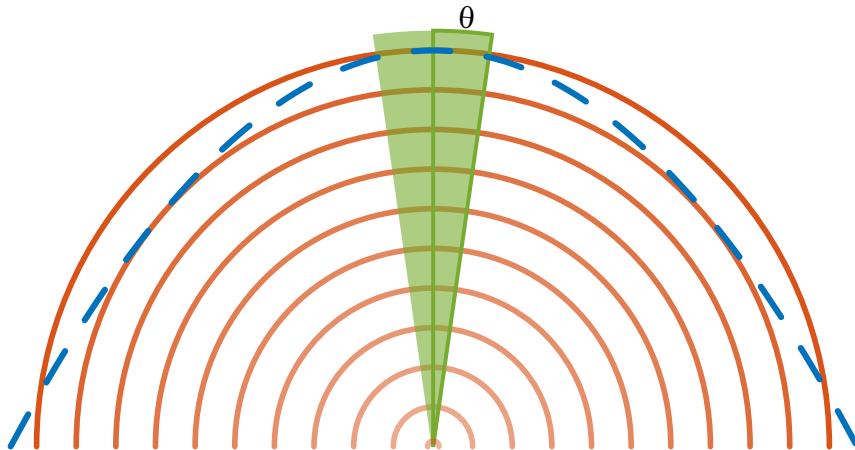


Figure 2.2: Small angle approximation. Spherical wavefronts are at a small angle approximately parabolic (dashed blue line).

2.2 Gaussian beam

One useful beam profile often used in optics is the Gaussian beam. The Gaussian beam has a transverse intensity profile following a Gaussian distribution. It is derived by shifting a paraboloidal wave by an imaginary constant, jkz_0 , where $z_0 = \pi W_0^2/\lambda$ is the Rayleigh range. The result, shown in figure 2.3 becomes

$$A = \frac{A_1}{z} \exp(-jk \frac{(x^2 + y^2)}{2z}) \xrightarrow{z \rightarrow z + jz_0} A = \frac{A_1}{z + jz_0} \exp(-jk \frac{(x^2 + y^2)}{2(z + jz_0)}). \quad (2.27)$$

From this the Radius of curvature, $R(z)$, and the beam width $W(z)$ may be derived by representing $z + jz_0 = q(z)$, which is the q parameter, and $1/q(z) = 1/r(z) - j \frac{\lambda}{\pi W^2(z)}$. The q parameter is a useful and simplistic way to represent a Gaussian beam, and it will prove to contain all the information needed about the Gaussian beam. When the substitution is made the Gaussian beam can be represented as its complex envelope:

$$U(\mathbf{r}) = A_0 \frac{W_0}{W(z)} \exp(-\frac{\rho^2}{W^2(z)}) \exp(-jkz - jk \frac{\rho^2}{2R(z)} + j\zeta(z)) \quad (2.28)$$

where all parameters have a meaning connected to the physical properties of the beam. W_0 is the smallest size of the beam, the beam waist, $\zeta(z)$ is a phase term, ρ is the radial position defined as $\rho^2 = x^2 + y^2$ and z is defined as the distance from the beam waist.

Beam Parameters

The parameters in equation 2.28 are often referred to as the beam parameters. They correspond to the physical properties of the beam, but also to each other in a convenient way. Without derivation the relationships are

$$\text{Beam Waist: } W_0 = \sqrt{\frac{\lambda z_0}{\pi}}, \quad (2.29)$$

$$\text{Beam width: } W(z) = W_0 \sqrt{1 + (\frac{z}{z_0})^2}, \quad (2.30)$$

$$\text{wavefront Radius of Curvature: } R(z) = z[1 + (\frac{z_0}{z})^2], \quad (2.31)$$

$$\text{Gouy phase: } \zeta(z) = \arctan(\frac{z}{z_0}). \quad (2.32)$$

All quantities are connected to the Rayleigh range, z_0 . For the wavefront radius of curvature and the Gouy phase this is plotted in figure 2.4. If two parameters of the beam are known, this is sufficient to properly describe the entire beam [5]. If the position z along with the Rayleigh range z_0 are known, then it is obvious that the q-parameter from the previous section can be used to completely describe the beam. Since $W(z)$ depends on z , the beam changes size as it propagates. This means that the beam is diverging when $z > 0$ or converging when $z < 0$. This can be described by the *divergence angle* $2\theta_0$, depicted in figure 2.3, which depends on the waist size and laser wavelength;

$$2\theta_0 = \frac{4}{\pi} \frac{\lambda}{2W_0}. \quad (2.33)$$

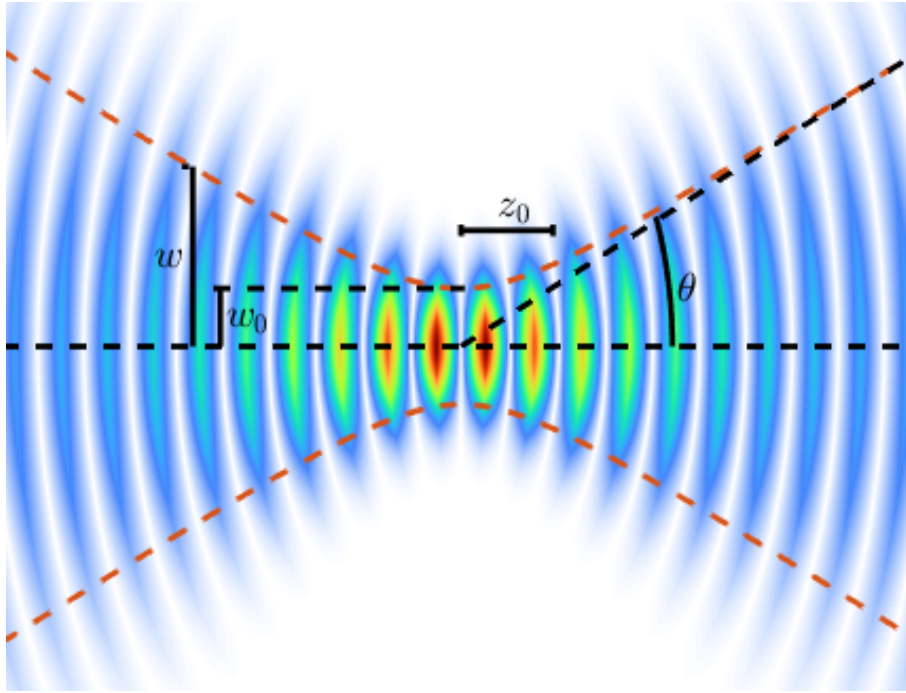


Figure 2.3: Wave-fronts of a Gaussian beam. The red line in the figure is the beam width, $W(z)$. Marked is the beamwaist, W_0 , the beam divergence θ_0 and the Rayleigh range z_0 . Note that the wavefronts are almost planar close to the waist. At the Rayleigh range the wavefront curvature is the largest, i.e. the radius of curvature is the smallest, and far outside of the Rayleigh range the curvature resembles that of a spherical wave with origin at the waist.

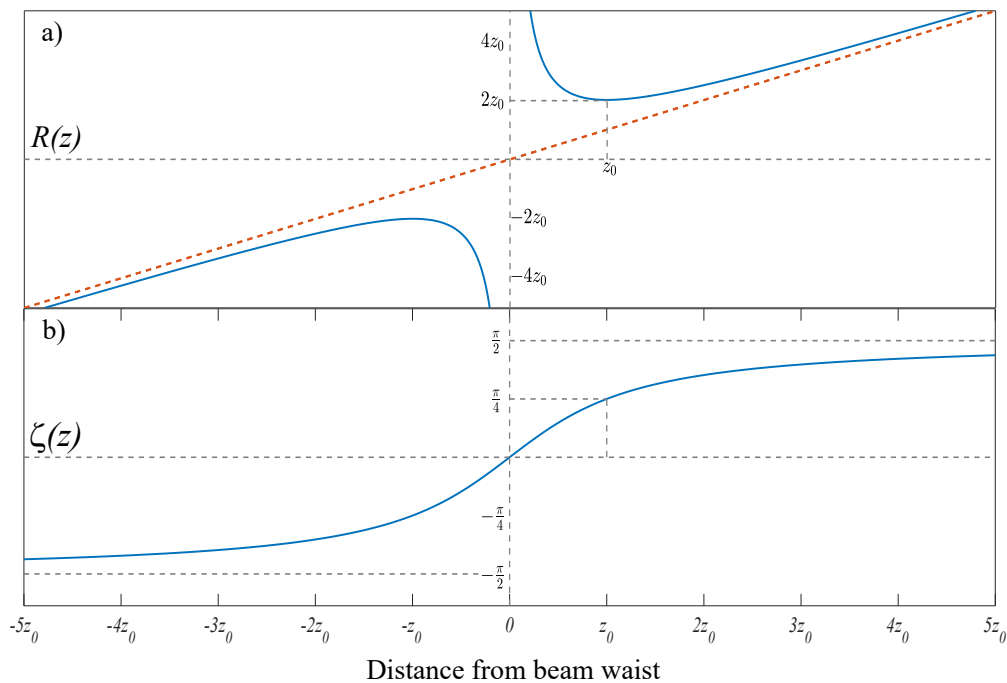


Figure 2.4: a) Radius of curvature of the wavefronts of a Gaussian beam as function of position along the beam axis. b) Gouy phase of a Gaussian beam as function of position along the beam axis.

An important observation is that a smaller beam waist has a greater divergence [5].

The physical properties above describe the beam geometry, but when talking about laser beam the quantities power and intensity are most often of great importance. Optical intensity is defined $I(r) = |U(r)|^2$, plotted in figure 2.3, where U is the complex amplitude. The intensity varies as a Gaussian function of ρ , with the maximum amplitude I_0 which is directly related to A_0 as $I_0 = |A_0|^2$. The intensity at any position $r = (\rho, z)$ is then

$$I(\rho, z) = I_0 \left[\frac{W_0}{W(z)} \right]^2 \exp\left(-\frac{2\rho^2}{W^2(z)}\right) \quad (2.34)$$

which is just the absolute of equation 2.28 to the power of 2, and shown for some different positions along z , with the on axis intensity in figure 2.5. This seems simple enough, but caution is advised when handling electrical field amplitude as A_0 , because the complex envelope is derived from the optical intensity and not from the electrical field. The electric field amplitude, E_0 relates to the complex field amplitude A_0 as $A_0 = \frac{E_0}{\sqrt{2\eta}}$ making $I_0 = \frac{|E_0|^2}{2\eta}$ where η is the impedance of the medium in which the intensity is considered. The impedance is related to refractive index as $\eta = \frac{\eta_0}{n}$ where η_0 is the impedance of free space and n is the refractive index [5],

The power is related to the intensity by taking the integral of the intensity over any transverse plane at some position z

$$P = \int_0^\infty I(\rho, z) 2\pi\rho d\rho \quad (2.35)$$

which is true for any radially symmetric beam intensity profile, but becomes

$$P = \frac{1}{2} I_0 \pi^2 W_0^2 \quad (2.36)$$

for a Gaussian beam.

In reality there are no perfect Gaussian beams, but most laser beams are "sufficiently" Gaussian and the approximation most often holds. When handling such approximation it is good to be able to quantify *how* Gaussian the beam is. Thus, the M^2 factor is introduced as the ratio of the waist-diameter-divergence product of the real and ideal beams;

$$M^2 = \frac{2W_m 2\theta_m}{2W_0 2\theta_0}. \quad (2.37)$$

Optical Components and Matrix representation

The formalism of Gaussian beams can be used to describe propagation of light through optical components. A Gaussian Beam incoming towards a focusing element will remain a Gaussian beam, but with modified properties. At the focus the new waist will be found, $z' = 0$ and the focus size will be $2W'_0$. A Gaussian beam reflected against a flat mirror remains the same, but changes its direction of propagation. If the mirror is instead focusing, a focus is created. One case that will be important in the section, regarding optical resonators, is when the curvature of the mirror R is equal to the negative curvature of the beam $-R_1$. Consider

$$\frac{1}{R_2} = \frac{1}{R_1} + \frac{2}{R} \quad (2.38)$$

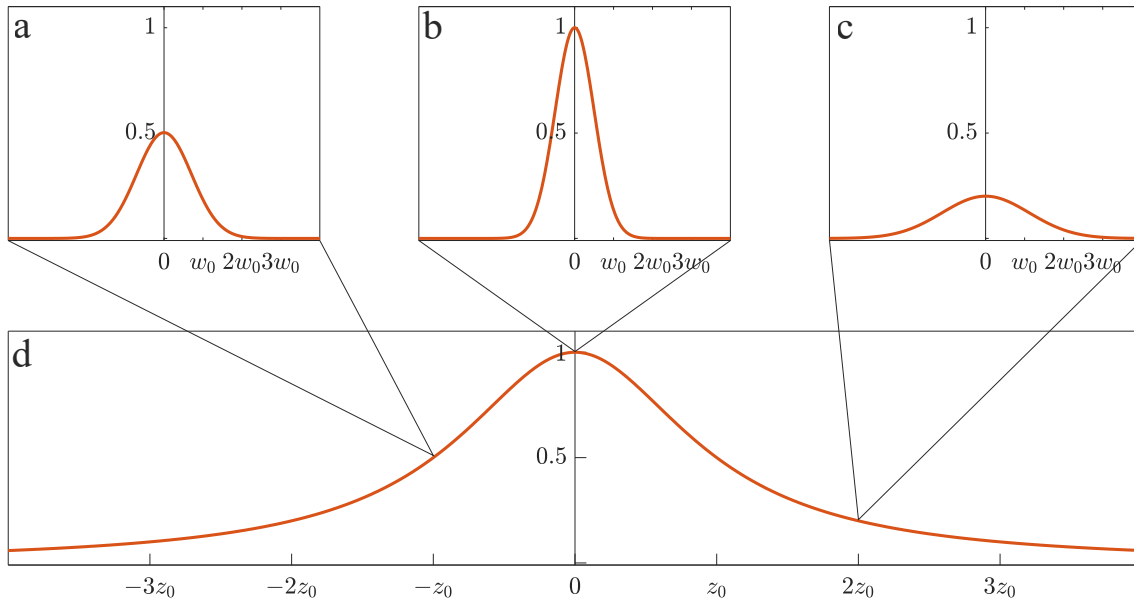


Figure 2.5: Normalized beam intensity I/I_0 of a Gaussian beam as a function of x at a) $z = 0$, b) $z = z_0$ and c) $z = 2z_0$. In d) the normalized intensity is plotted as a function of z when $x=y=0$, often called on axis intensity.

where R_2 denotes the radius of curvature of the reflected beam. Using $R_1 = -R$ will then yield $\frac{1}{R_2} = \frac{1}{R}$ and the wavefront radius of curvature has changed sign, but the absolute value of it remains the same. A converging beam thus becomes diverging and vice versa. The beam remains the same but with altered direction, causing it to retrace itself. This can be compared to a lens placed at the distance $2f$ from a diverging source, the lens will refocus at a distance $2f$ from it.

A convenient way to perform those calculations is given by Matrix Optics. Any optical element can be represented by a Matrix

$$\mathbf{M} = \begin{pmatrix} A & B \\ C & D \end{pmatrix}, \quad (2.39)$$

which may simplify calculations significantly. The letters A, B, C & D depend on the optical element, and govern how the beam is altered. Conveniently, the ABCD Law for a gaussian beam is defined

$$q_2 = \frac{Aq_1 + B}{Cq_1 + D} \quad (2.40)$$

where q_1 and q_2 are the q-parameters of the incoming and outgoing beam. When handling large optical systems with multiple components each component is described by a matrix - including free space - and those matrices may then be multiplied together as $\mathbf{M} = \mathbf{M}_n \cdot \mathbf{M}_{n-1} \cdot \dots \cdot \mathbf{M}_1$. This allows rapid calculation of how a beam transforms inside of an optical resonator, and is useful when determining what eigenmode the resonator has [10].

2.3 Ultrafast Optics

As when considering the propagation in space, an optical pulse has a complex amplitude $U(r, t)$. Forgetting about space this becomes $U(t)$, which is commonly written in the form $A(t) \exp(j\omega_0 t)$, where $A(t)$ is the complex envelope and the central angular frequency ω_0 is related to the central frequency by $2\pi\nu_0$. The magnitude is determined by $|A(t)|$, and the complex envelope contains an additional phase term $\varphi(t)$ so that $U(t) = |A(t)| \exp(j(\omega_0 t + \varphi(t)))$. The time varying magnitude describes the shape of the pulse, and returns the time dependent intensity when squared $I(t) = |A(t)|^2$.

The pulse temporal profile depends on the time dependency in $|A(t)|$, and if $A(t)$ is a Gaussian function the pulse is Gaussian in the time domain. There are a large number of different shapes, but the Gaussian is the most common approximation. A Gaussian pulse, $\exp(-2t^2/\tau^2)$ has a temporal width τ , which can be compared to the waist of the spatial Gaussian profile.

To obtain pulsed light at all, it is necessary to have several optical frequencies present. They then interfere with each other in time, as illustrated in figure 2.6. As

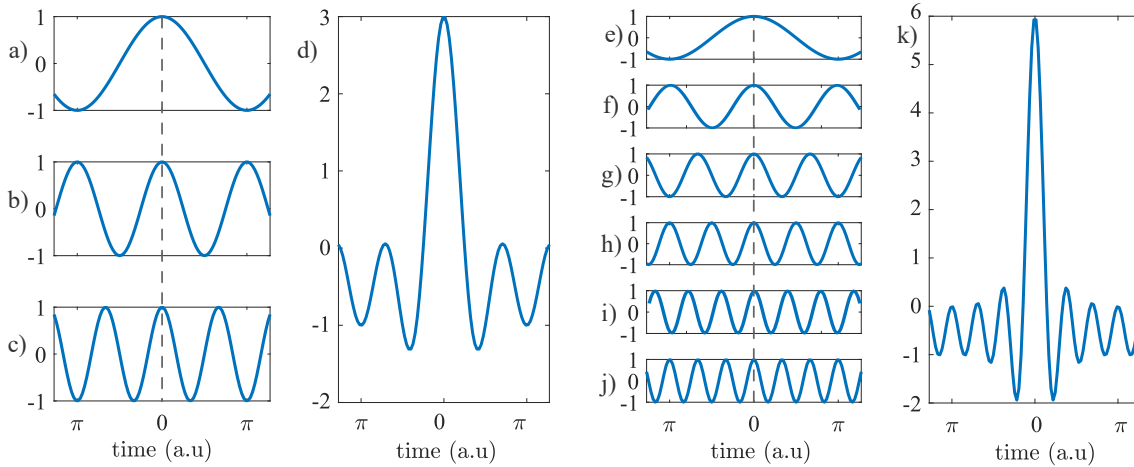


Figure 2.6: Illustration of the relationship between time and frequency. In (a-c) and (e-j) cosine-functions are plotted as a function of time. The dashed line indicates the initial phase. In figure d) and k) the sum of (a-c) respective (e-j) have been plotted. Considering the width of the central peak it is visible that d), a sum of three frequencies is wider than k), with six frequencies and twice the spectral width.

seen in the figure, including more frequencies allows for a shorter time duration. This relates to the time-frequency Fourier relation, where a spectral complex amplitude $V(\nu)$ is described by the Fourier transform of the complex amplitude $U(t)$. If $V(\nu)$ is narrow, it's inverse Fourier transform is wide - making $U(t)$ wide which corresponds to τ being large. Analogously, if $U(t)$ is very narrow with a small τ , then the Fourier transform $V(\nu)$ must be wide, and the spectral width $\Delta\nu$ is large. In both domains there is a phase, $\varphi(t)$ and $\psi(\nu)$.

If the phases are constant, the pulse is so called Fourier limited. This means the product between the pulse duration τ and the spectral width $\Delta\nu$ is the smallest possible. Using the Full Width Half Maxima (FWHM) the smallest value is $\Delta\nu\tau_{FWHM} = 0.44$ for a Gaussian temporal profile, while other temporal profiles

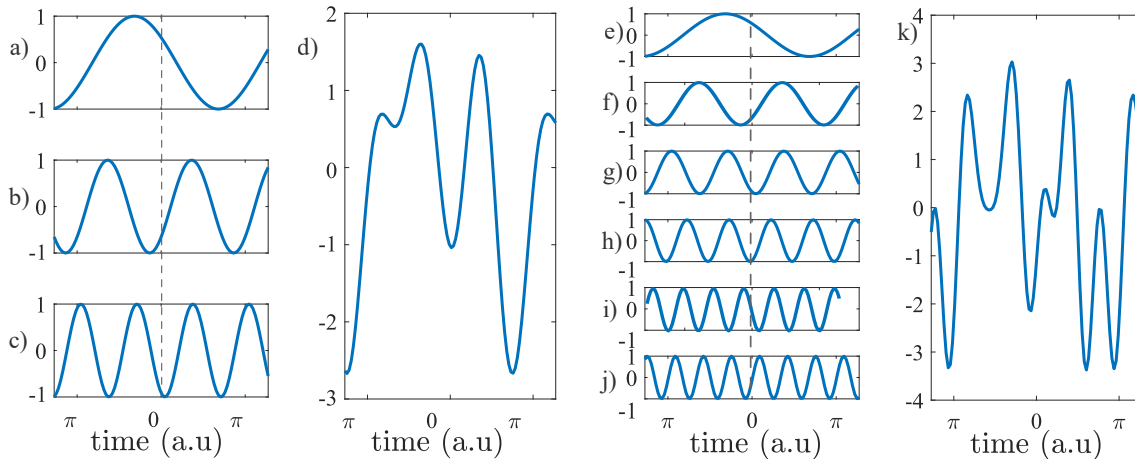


Figure 2.7: Illustration of the relationship between time and frequency. In (a-c) and (e-j) cosine-functions are plotted as a function of time, with an additional phase term φ . The dashed line indicates the initial phase. In figure d) and k) the sum of (a-c) respective (e-j) have been plotted. In both cases the pulses have been widened compared to figure 2.6, and the shape is deformed.

have different time-bandwidth products. This corresponds to the frequency of the optical field being the same at all times in the pulse.

When the phase is not constant, neither is the frequency. Instead an instantaneous frequency can be defined as $\nu_i = \nu_0 + \frac{1}{2\pi} \frac{d\varphi}{dt}$, where ν_0 is the central frequency. A linear phase in time corresponds to a constant frequency shift, meaning the frequency is the same at all times, but it is not the central frequency. If the phase is instead quadratic, $\varphi = at^2/\tau$, where a is a constant, its derivative will be a linear function and the pulse will have an instantaneous frequency with a linear time dependence. This means the pulse is linearly chirped. Depending on if the instantaneous frequency goes from red to blue or blue to red the pulse is said to be up-chirped or down-chirped. In a pulse with chirp the frequencies are separated in time, which results in a stretching of the pulse in the time domain illustrated in figure 2.7

A pulse that propagates through a material will be affected by the material. Dispersion in the material will cause different frequencies to travel at different speed, as the frequencies experience different refractive indices. This can be described by defining a propagation constant $\beta = 2\pi\nu n(\nu)/c_0$. If the pulse is considered as a whole it then propagates with a group velocity, $v_g = 1/\beta'$ where β' is the derivative of β with respect to the angular frequency. The second derivative of β is the group velocity dispersion $\beta'' = d^2\beta/d\omega^2$. A material with a frequency dependent refractive index thus induces a parabolic phase on the pulse, chirping the pulse. Common transparent materials induce a positive GVD in the wavelength range of interest 500 nm to 1000 nm (visible to near infrared), up chirping the pulse. There are regions of negative GVD, instead down chirping pulses, but such regions will not be considered in this work. There are more complex frequency dependencies of the refractive index, but those are typically small and will be left for the reader to explore.

There are ways to combat the chirp and re-compress the pulse in time. What needs to be done is effectively to put the different frequencies back in phase. This

can be done using gratings or prisms, by separating the frequencies in space and then letting them propagate different distances before recombining them. This can also be done using chirped mirrors, inducing a negative GVD to compensate for an up-chirped pulse. To compensate for a down-chirp in the visible spectrum it is often enough to insert a small amount of dispersive material, as common materials have normal dispersion.

2.4 Nonlinear Optics

The wave equation as it is presented previously makes an assumption on the induced material polarization, \mathcal{P} . Namely, that it is linear. While this holds for low intensities it is an approximation that breaks down for higher intensities. In general it can be said that the polarizability of a material is some unknown function $\mathcal{P} = f(E)$. While the function is unknown, close to zero it can be expanded using its Taylor approximation

$$\mathcal{P}(t) = \epsilon_0(\chi^{(1)}\mathcal{E} + \chi^{(2)}\mathcal{E}^2 + \chi^{(3)}\mathcal{E}^3 + \dots) \quad (2.41)$$

where $\chi^{(1)}$ is the linear susceptibility, and $\chi^{(2)}$ and $\chi^{(3)}$ are the second and third order nonlinear susceptibilities [7].

There is a qualitative explanation of the linear refractive index, based on the material polarization and electric fields inducing dipoles in materials. If the electric field is oscillating, the dipoles also oscillate. This means there are accelerating charges in the material, oscillating with the incoming light (both in phase and with the same frequency). A fraction of the energy in the light induces a small oscillation, which in turn generates a wave that is identical to the incoming light. There are several dipoles at various different positions and the incoming light interfere with the light radiating from all oscillating dipoles, resulting in a phase delay, as if the light had propagated further than the geometrical distance. This is of course the refractive index, related to $\chi^{(1)}$ as $n_0 = \sqrt{\frac{\epsilon}{\epsilon_0}} = \sqrt{1 + \chi^{(1)}}$ [5]. This relates to the wave equation, where the Polarisation term represents a source term.

The same reasoning can be used to qualitatively describe nonlinear optics phenomena. The polarization P governs the oscillation, and as the polarization becomes nonlinear so does the oscillation. In a simple manner, second order effects can only occur in media which break the symmetry of the polarisation. Otherwise the generated light will look identical but phase shifted by π causing the light to cancel via destructive interference. The same is true for all even order nonlinearities [5].

In this work the material of interest is amorphous fused silica, which is centrosymmetric and therefore has no even order nonlinearities. With this motivation, $\chi^{(2)}$ will be completely excluded henceforth. To observe third order nonlinear effects this is often a necessity, as the second order effect is much stronger. A polarisation curve with $P = P_L + P_{NL} = \epsilon_0(\chi^{(1)}E + \chi^{(3)}E^3)$ is shown in figure 2.8.

Putting this into the wave equation, the nonlinear wave equation, or the nonlinear Schrödinger equation, is obtained;

$$\nabla^2 E + \frac{1}{c} \frac{\partial^2}{\partial t^2} E = \frac{1}{\epsilon c^2} \frac{\partial^2}{\partial t^2} (P_{NL}) \quad (2.42)$$

$$\nabla^2 E + \frac{1}{c} \frac{\partial^2}{\partial t^2} E = \frac{1}{\epsilon c^2} \frac{\partial^2}{\partial t^2} (\epsilon_0 \chi^{(3)} E^3) \quad (2.43)$$

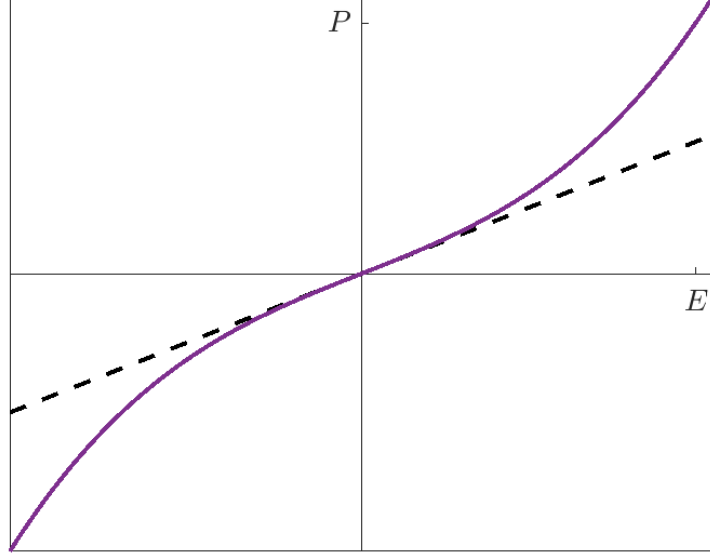


Figure 2.8: The figure shows polarisation, P , dependence on electric field amplitude, E . Close to zero, the behaviour is linear, black dashed curve, while at stronger fields the behaviour is dominated by the third order term.

where E is the electric field dependent on time. There are two main effects that are the focus of this thesis, Self Focusing and Self Phase Modulation (SPM). Both effects arise due to a third order effect, the intensity dependent refractive index, $n = n_0 + n_2 I(r, t)$, where n_2 is called the nonlinear refractive index.

2.4.1 Self Focusing

As suggested by the name, self focusing is when a laser beam is focused by itself. The following version of the nonlinear Schrödinger Equation follows from 2.43 when assuming a monochromatic wave, as in [11]

$$\frac{\partial A}{\partial z} = -\frac{j}{2k} \nabla_{\perp}^2 A - \frac{jk n_2}{2} |A|^2 A, \quad (2.44)$$

where A is the complex amplitude, k is the wavenumber and n_2 is the nonlinear refractive index. The relationship between complex amplitude and intensity is $|A|^2 = I$. Here, paraxial approximation and slowly varying envelope approximation have been applied, along with the nonlinear polarization, to the wave equation. The slowly varying envelope approximation assumes no fast variation in the amplitude along the propagation direction, such as for a continuous field.

The first term describes how the complex amplitude A varies along propagation direction z , the second term is the diffraction term and the final term describes nonlinear propagation. To simplify momentarily the diffraction is excluded from reasoning. The equation then becomes $\partial_z A = -jkn_2 IA/2$, using $I = |A|^2$, and the nonlinearity corresponds to an intensity dependent phase, or an intensity dependent refractive index, $n = n_0 + n_2 I$. Considering only n_2 and a Gaussian input profile at the surface of a medium, as in figure 2.9 the intensity variation of the beam

induces a refractive index gradient. As the beam propagates through the medium, accumulating different phases depending on position, just as in a lens.

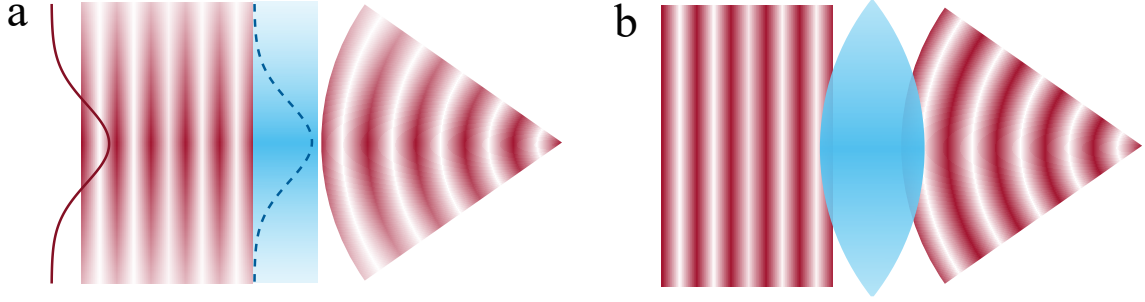


Figure 2.9: An illustrative comparison between a) self focusing in a thin piece of nonlinear material and b) focusing from a lens.

While self-focusing occurs if the induced refractive index gradient is sufficient, this is not the case for catastrophic self-focusing: when the beam collapses. Mathematically it collapses into a single point, but in reality the intensity becomes high enough to ionize materials, and for other nonlinear effects to occur. The only requirement for self focusing to become catastrophic is that diffraction is cancelled out. As diffraction depends of the beam size at the waist w_0 , a large w_0 results in a long diffraction length. With a longer diffraction length a much smaller intensity required to compensate for the diffraction effect. In [12] the diffraction length is the Rayleigh range z_0 , but other definitions are used in previous work, then as $L_{DF} = 2z_0$ [11, 13, 14] while the characteristic length for self focusing is

$$L_{SF} = \frac{1}{n_2 k_0 I_0} \quad (2.45)$$

defined by the accumulated nonlinear phase being one [12]. For self focusing to occur, L_{SF} needs to be shorter than the diffraction length. A lower limit is when $L_{SF} = z_0$, from which the following can be deduced:

$$L_{SF} = z_0 \longleftrightarrow \frac{z_0}{L_{SF}} = 1 \quad (2.46)$$

$$\text{insert definition of } L_{SF} \text{ and } z_0, \text{ and use } \pi w_0^2 I_0 / 2 = P \quad (2.47)$$

$$1 = \frac{\pi n_0 n_2 w_0^2 k_0 I_0}{\lambda_0} = \frac{2\pi^2 n_0 n_2 w_0^2 I_0}{\lambda_0^2} = \frac{4\pi n_0 n_2 P}{\lambda_0^2}. \quad (2.48)$$

$$(2.49)$$

This shows that rather than depending on intensity, catastrophic self focusing depend on beam power. If the power of a beam is larger than the critical power

$$P_{cr} = \alpha \left(\frac{\lambda^2}{4\pi n_0 n_2} \right) \quad (2.50)$$

it collapses due to self focusing, regardless of beam size and peak intensity. The parameter α is a constant depending only on the intensity profile, and is for a Gaussian intensity distribution 1.8962. The lowest value of the parameter is 1.862 25, found for the so called Townes profile [15].

The Townes profile is the numerical solution to the stationary nonlinear Schrödinger equation, where $\partial_z A = 0$. This corresponds to the beam profile A having identical transverse cuts at any position z_n . It is also important as a Gaussian beam propagating in a bulk medium at a power close to the critical power will first undergo reshaping, before self focusing or diffracting [16]. This effect often cause the beam to gain a smoother spatial profile, therefore often being referred to as mode self-cleaning [12].

If the beam power is higher than the critical power of a long medium, the self focusing will eventually become catastrophic and the beam will collapse. In reality self focusing is limited by other effects, such as plasma defocusing or multi-photon absorption, but this still induces damage in the material and a loss of power. The point of collapse is semi-empirically found to be

$$L_C = \frac{0.367z_0}{\sqrt{(\sqrt{\frac{P}{P_{cr}}} - 0.852)^2 - 0.0219}} \quad (2.51)$$

for a Gaussian spatial profile, entering the nonlinear material at the waist [12].

While the occurrence of self focusing is governed by the power ratio between beam power and critical power, the effect is also dependent on the intensity profile. As mentioned above, different beam profiles have different critical powers [15]. As the power to critical power ratio increases, irregularities in the beam profile can induce what is known as small scale self focusing. As the beam undergoes self focusing the different irregularities may self focus separately, causing them to grow. As the irregularities grow they gain power, and the end result is several filaments of powers comparable to the critical power. The different filaments can then collapse separately or lose power due to various effects, such as plasma defocusing or nonlinear absorption [12].

Also this process depends on the beam intensity profile. A random noise on a Gaussian beam will induce a random beam break up, but there are profiles that show a very regular behaviour. One example is vortex beams, that break up into rings depending on vortex order and power to critical power ratio [17]. Other beam profiles have been object of study, such as necklace beams consisting of a ring of Gaussian profiles [18]. Small-scale self-focusing is illustrated in figure 2.10, inspired from [19], where the modulation in a is enhanced after propagation through a nonlinear media.

2.4.2 Self Phase Modulation

For pulsed light, the intensity profile is time dependent. If the intensity is time dependent, so is the refractive index $n = n_0 + n_2 I(t)$ as introduced in section 2.4, which means that the nonlinear phase accumulation also becomes time dependent [7].

The nonlinear phase is defined $\Delta\varphi = -n_2 I(t) k_0 z$, and different amount of phase is accumulated at different times. A light pulse with an additional phase have an instantaneous frequency,

$$\omega_i = \omega_0 + \frac{d\varphi}{dt} \quad (2.52)$$

as discussed in section 2.3.

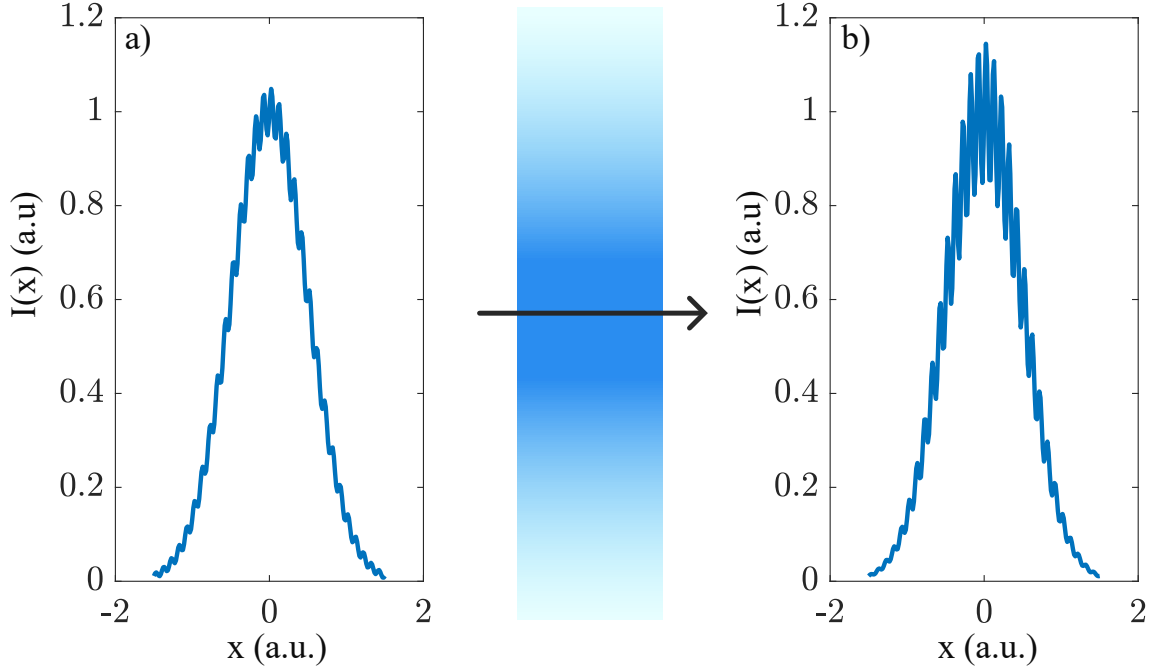


Figure 2.10: A beam with some modulation or noise (a) that propagates in a nonlinear media may undergo small scale self focusing, enhancing the structures in the beam (b). Eventually this causes the beam to breakup into multiple filaments.

Consider a positive nonlinear refractive index n_2 and a Gaussian temporal intensity profile, as in figure 2.11. At the leading edge, early times, the derivative of the intensity is positive and the nonlinear phase gives a negative contribution to the instantaneous frequency, $\Delta\omega_i = \omega_0 - n_2 k_0 z dI(t)/dt$. Thus $\omega_i < \omega_0$, and energy is taken from the central frequency to new lower frequencies. At the trailing edge the opposite is true, and instead an increase of instantaneous frequency is seen. This is illustrated in figure 2.11. The largest frequency shift is obtained where the derivative is the steepest, for a Gaussian, this is the case approximately at the centre of the edge.

As the instantaneous frequency is changed, intensity is moved from one frequency to another. This can result in a wider spectral width, but also in growth of the small wings. The above reasoning holds for Fourier limited pulses, where the instantaneous frequency is constant through the pulse. For chirped pulses the instantaneous frequency is not constant but varies with time according to the chirp of the pulse. For a linearly chirped pulse the instantaneous frequency is $\omega_i = \omega_0 + \frac{2at}{\tau^2}$, and this is then further modified by the nonlinear phase. If the pulse is upchirped it can still broaden as the lower frequencies at the leading edge are further decreased while the higher frequencies at the trailing edge are increased. A downchirped pulse instead has an instantaneous frequency that varies from high to low, but the same temporal intensity profile. This means the higher, leading, frequencies are decreased while the lower, trailing frequencies are increased, which results in a spectral narrowing.

Just as there is a spatial soliton due to self focusing, there is a temporal soliton due to SPM. A temporal soliton has the same temporal profile at all times. While this is already true for a pulse in vacuum, a pulse in a dispersive material will be chirped. The instantaneous frequency then varies linearly with time, and frequencies

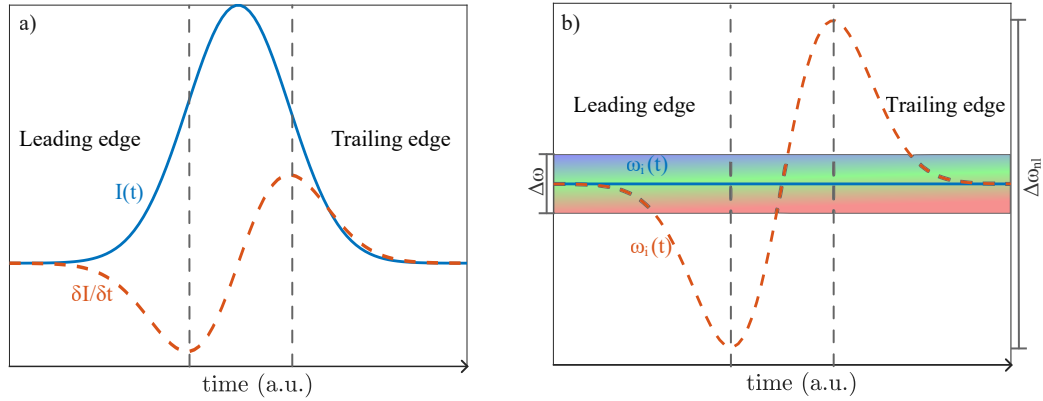


Figure 2.11: Illustration of Self Phase modulation of a Gaussian pulse. In a) the temporal intensity is shown as a function of time (blue line) along with its derivative (red dashed line). In b) the instantaneous frequency of a FTL pulse is plotted (blue line) along with the pulse initial spectral width. The red dashed line is the instantaneous frequency due to SPM.

separate from each other. If the instantaneous frequency were to remain the same all through the pulse the trailing and leading edge would propagate with the same speed and the stretching would not occur. This can happen if dispersion and SPM are present at the same and cancel each other out. For this to happen the dispersion needs to be anomalous, which is not the case for visible light in common materials where the dispersion is normal.

2.5 Multi-Pass cell

2.5.1 Resonator Optics

When a wave with a spherical phase hits a spherical mirror with the same radius of curvature the reflected wave is refocused into itself. If a beam that is retracing itself is met with another mirror, again with the same radius of curvature, it will again retrace itself. This way the beam will propagate back and forth between the two mirrors, retracing itself on each roundtrip. This is a simple description of a beam confined in an optical cavity. There are certain conditions that must be fulfilled in order for the beam to remain in the cavity - resonator modes and stability.

The resonator modes mainly depend on the cavity length and the phase accumulated during propagation in the cavity. For a wave to be a mode of a cavity it needs to retrace itself, meaning it needs to be identical when it starts a round trip and when it ends a round trip. For the beam to look the same at the start and end of the round trip it needs to accumulate a phase of 2π . Otherwise destructive interference will destroy the beam [5].

Stability is what keeps the beam inside of the cavity and relates to both the length of the cavity and the radius of curvature of the mirrors. For each mirror a stability parameter is defined as $g = 1 - \frac{L}{R}$. The cavity stability is given by the product of the two stability parameters. If the product is between 0 and 1 the cavity

is stable,

$$0 \leq g_1 g_2 = \left(1 - \frac{L}{R_1}\right) \left(1 - \frac{L}{R_2}\right) \leq 1 \quad (2.53)$$

and the relation is known as the stability condition [5].

2.5.2 Multi-Pass cells for Post compression

The output of a laser has a certain minimum pulse duration, the Fourier transform limit (FTL), as discussed above. At times, this FTL, is not sufficiently short and schemes to further shorten the pulse in time is necessary. To do this the spectrum must be broadened via nonlinear effects, such as super continuum generation or self phase modulation (SPM). The later is what is used in the Multi-pass cells for post compression of ultrashort laser pulses [1, 20].

In short, an MPC consist of a nonlinear medium inside an optical resonator. Originally the scheme was applied in absorption spectroscopy applications, where multiple passes through a medium allowed for the detection of specimen with lower concentration. The principle of the MPC for post compression is the same - a laser pulse is propagated several times through a nonlinear material while continuously being re-focused. This way, the nonlinear spectral broadening can become large while other effects resulting in beam degradation can be avoided.

2.5.3 The Herriott Configuration

The geometry is the first part to consider. Most common is the Herriott-type MPC, based on a Herriott Cell originally implemented for absorption spectroscopy [21]. The scheme consist of two mirrors forming an optical cavity, in which the transverse eigenmodes propagate off axis. This results in a periodic pattern on the cavity mirrors, as shown in figure 2.12 b).

If the cavity is represented by an equivalent resonator - that is replacing the mirrors with a series of lenses with the same focusing properties, illustrated in figure 2.12 c) - the periodic system has a sinusoidal advance in the transverse x and y positions. In the cavity this results in a circular pattern where two consecutive passes are displaced from one another, by an angular advance ξ . As the system is periodic, after some number of round-trips, N , the total angular advance ξN is equal to some integer multiple of 2π . When this happens, the beam has returned to its original position and the re-entrant condition

$$\xi N = 2\pi k, \text{ where } k = 1, \dots, N - 1 \quad (2.54)$$

is fulfilled. For a radius of curvature R and a fix number of round-trips N the integer k determines the cell length [22]. The angular advance is equivalent to the Gouy phase accumulated during one round trip ζ_{RT}

$$\zeta_{RT} = \tan^{-1}\left(\frac{z_2}{z_R}\right) - \tan^{-1}\left(\frac{z_1}{z_R}\right) = \xi = \frac{2\pi k}{N} \quad (2.55)$$

. This is proven geometrically in [22].

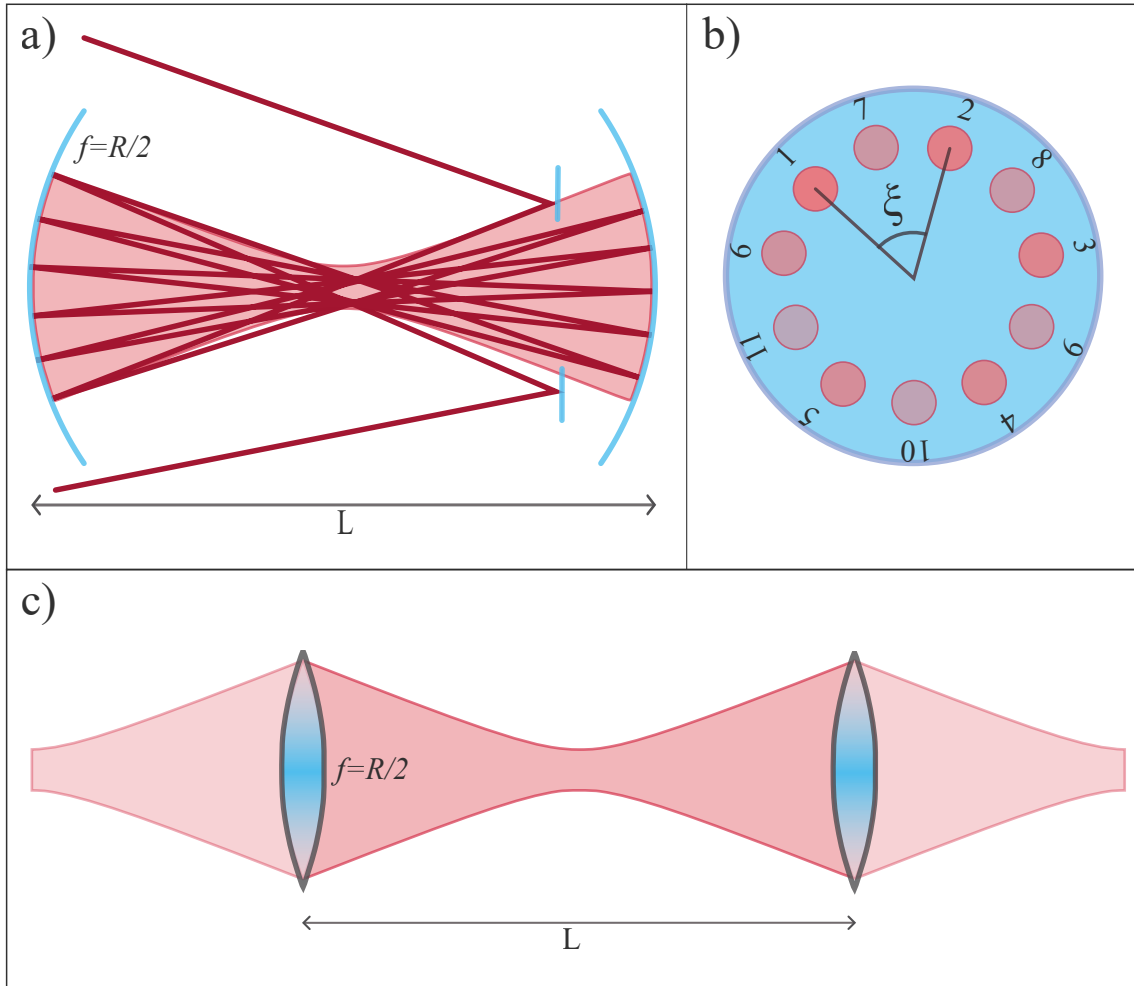


Figure 2.12: a) Schematic of a traditional MPC set-up, without the nonlinear medium, where the beam propagates of axis in an optical resonator with two identical focusing mirrors. b) The Herriott pattern on one of the mirrors, when the reentrant condition is fulfilled for $N = 11$. c) Periodic sequence of lenses representing a Herriot cell equivalent resonator.

2.5.4 Nonlinear phase

An MPC used for post compression requires a nonlinear medium. Either a gaseous medium can be chosen, or a bulk medium. Each have limitations and advantages, but both lead to a nonlinear phase accumulation. To quantify the nonlinear phase the B-integral is defined as the nonlinear phase accumulated on axis, using nonlinear refractive index n_2 and $I_p(z)$ denoting peak intensity on the optical axis,

$$B := \frac{2\pi}{\lambda} \int n_2 I_p(z) dz. \quad (2.56)$$

$$(2.57)$$

The B integral is related to the nonlinear phase treated in section nonlinear optics, but taking into account that a pulse varies in space. There is no time dependence in the B-integral, but it describes the nonlinear phase that the pulse accumulates on axis. This needs to be sufficiently low, as the beam may otherwise self focus catastrophically rendering the MPC useless. In gas this caps the Power, as a beam power above the critical Power for self focusing causes the beam to at some point collapse. For bulk material the cell can still support high power to critical power ratios [23], but it is not completely understood what it is that allows this. In a bulk MPC the nonlinear medium can be very thin, and the beam propagates in free space and is refocused before being re-inserted into the nonlinear medium. This appears to play some role in halting the catastrophic collapse of the beam.

To quantify the spectral broadening from an MPC the input spectral width $\Delta\omega_{in}$ is compared to the output spectral width $\Delta\omega_{out}$ as below,

$$b = \frac{\Delta\omega_{out}}{\Delta\omega_{in}} = \sqrt{1 + \frac{4}{3\sqrt{3}}\phi_{max}^2} \quad (2.58)$$

where ϕ is the maximum nonlinear phase shift, for a Gaussian beam $B = 2\phi_{max}$ [22].

While the broadening is necessary to reduce the Fourier Limit of the pulse, the compression also depends on the chirp acquired during nonlinear propagation. If the chirp is not linear, meaning the spectral and temporal phase is not quadratic, there may be complications. To compress the pulse the chirp needs to be compensated, and typically the linear chirp is what is compensated for. Thus there is a compression ratio defined as

$$K := \frac{\tau_{FWHM,in}}{\tau_{FWHM,out}} \quad (2.59)$$

where the FWHM of the input pulse is divided by the FWHM of the output pulse [22].

2.5.5 Convex Concave MPC

As briefly mentioned above, there are limitations when design an MPC. In addition to the mentioned catastrophic self focusing, there are several problems to take into account, such as mirror damage thresholds (the maximum fluence accepted by the mirror), resonator stability and ionization intensities. Sometimes the problems can be combated by the choice of nonlinear medium. A gas MPC with a focus in the middle, as in figure 2.12 a), can lead to problems, if the focus intensity is high enough to ionize the gas.

To lower the intensity on the mirrors they are usually moved further away from the focus. This results in very long cavities of several meters. A recently proposed solution by the groups of Saraceno and Pronin independently is the convex-concave scheme [3, 4]. An optical resonator is formed using a defocusing mirror and a focusing mirror. This is realized with nonlinear medium being gas (air) [3] or bulk (fused silica) [4] respectively. Both cells are short, 61.5 cm ($R_1 = 2.5$ m, $R_2 = -2$ m) respective 11.4 cm and 28.3 cm ($R_1 = 0.25$ m and 3 m, $R_2 = -0.2$ m and -1 m). The conclusion of both groups is that the scheme is successful and allows for increased pulse energies.

Chapter 3

Designing the MPC

3.1 Designing the MPC resonator

In this section the procedure of designing an MPC with the goal of broadening a Ti:Sapphire laser, while avoiding focusing the beam, is presented. Restrictions, calculations and results relevant for design choices that were made will be presented, and further related to the scope of the thesis investigating limitations of current MPC configurations. The starting point was based on at the time suggested, and now published, designs of a Convex-Concave (CXCVC) Herriot configuration by Saraceno and Pronin [3, 4], pictured in figure 3.5 a). It turned out that in the present case this was in fact not possible due to the restrictions that are placed on the problem in terms of maximum intensity, space and mirror budget.

The idea is to calculate a configuration consisting of one de-focusing (convex) mirror, and one focusing (concave) mirror, forming an optical cavity. Each mirror has a radius of curvature, meaning that the distance between the two determines the Gaussian beam which is an eigenmode to the cavity. To do this a first restriction needs to be considered - the intensity on the mirrors should be safely below the damage threshold of the mirrors. The limit was set to 1 TW cm^{-2} . Using the laser specifications and assuming a perfect Gaussian Beam, the minimum spot radius was calculated to $W_1 = 3.1 \text{ mm}$. By selecting a suitable radius of curvature on the convex mirror a cavity of a given length L could be calculated. The main limitation on L was available space in the lab, limiting it to less than 2.5 m. The next limitation is on mirror budget and delivery time. To minimize these, small radii of curvatures were chosen, ranging from 0.5 m to 4 m in absolute values, and the result of those calculations are shown in figure 3.1 a). Calculations were done also for larger values, that will be presented and shortly discussed.

Based on the designed cavities, the re-entrant condition was calculated, which was done using the Gouy phase accumulated between the two mirrors. The re-entrant condition, explained in detail in the theory, is

$$N\zeta_{RT} = q2\pi, \quad (3.1)$$

where N is the number of round-trips, ζ_{RT} is the accumulated Gouy phase over one round-trip and q is some integer, smaller than N . To find the periodic solutions, the Gouy phase was first divided by 2π , and then plotted as a function of cavity length, as seen in figure 3.1 b). If the value is equal to a fraction $\frac{q}{N}$, where q and

N are integers, the cavity is a periodic solution for N round trips. In the plot, one example is that the purple (RoC =4 m) line passes 0.02, which is $1/50$.

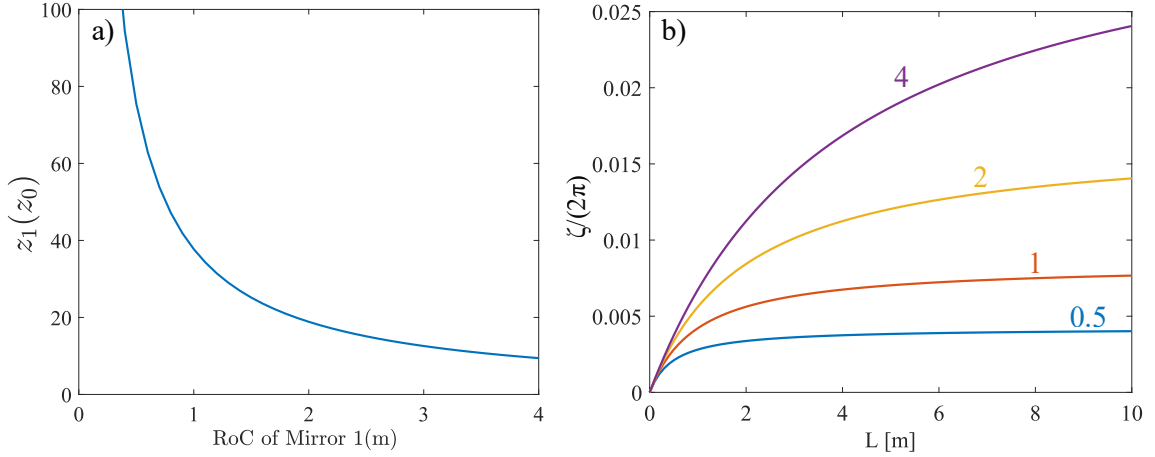


Figure 3.1: a) Position of defocusing mirror normalized to Rayleigh ranges as a function of RoC of defocusing mirror. The mirror is always placed far outside of the Rayleigh range. The Rayleigh range increases with RoC. b) shows accumulated Gouy phase per round trip normalized by 2π for different RoC of the defocusing mirror as a function of cavity length L . The Gouy phase per round trip is small, meaning a large number of round trips are required to fulfill the re-entrant condition. The purple curve is for RoC 4 m, and yellow, red and blue RoC: 2 m, 1 m and 0.5 m as noted in the figure.

As seen in the figure 3.1 the accumulated Gouy phase in a cavity far outside the rayleigh range, is small. This is also illustrated in figure 3.2, where the Gouy phase and Gaussian mode is also plotted, to illustrate that within the MPC the phase is flat. The direct consequence of this is that a large number of round trips would be required to satisfy the re-entrant condition, which is problematic as even with high reflectivity mirrors a part of the beam power is lost. To achieve the intended broadening, only a few round trips is required. For example, using a defocusing mirror with RoC 4 m with the intended mirror, 2" silver mirror, a large number of bounces would also not fit, as the bounces need to be spatially separated from each other. The intended application require as low losses as possible. 50 round trips require 50 bounces on each cavity mirror, which corresponds to a transmission of 33%. Finally, the cavity length would be 6 m, which is not possible to physically implement in the space at hand.

Calculations can be made to take the defocusing mirror closer to, or even inside of, the Rayleigh range, by increasing the RoC, as is done in figure 3.3. Even in this case the cavity becomes long for $N = 25$, and more round trips are required to reach a compact Herriot cell. To place the defocusing mirror close to the Rayleigh range very large RoC of the mirrors are required, and very long Rayleigh ranges. This is because of the behaviour of Gaussian beams, the connection between beam width W_z , beam waist W_0 and Rayleigh range z_0 . To move the defocusing mirror closer to the waist (or decreasing $z \propto z_0$) the waist needs to increase, and then also the Rayleigh range increases, with the square of the waist increase. The values for RoC 0.5 m, 1 m, 2 m and 4 m and larger RoC 10 m, 20 m and 40 m are presented in table 3.1. It should be noted that mirrors with long radii of curvature are hard to

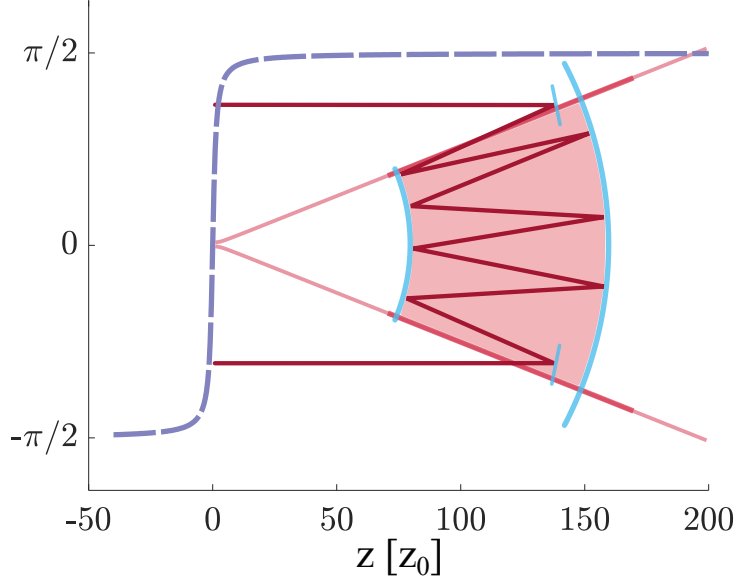


Figure 3.2: The figure shows the designed MPC with mirrors placed at $z_1 = 80z_0$ and $z_1 = 160z_0$ placed in a plot of the Gouy phase against z in units of z_0 . Within the MPC the Gouy phase is flat, meaning very little is accumulated.

produce, very expensive and have long delivery time.

Table 3.1: Mirror position, Rayleigh range, and waist size for different Radius of Curvature on the defocusing mirror.

RoC(m)	0.5	1	2	4	5	10	20	40
z_1 (m)	0.5	1	1.99	3.96	4.9	9.34	15.6	18.8
z_0 (m)	0.0066	0.026	0.11	0.42	0.65	2.48	8.28	19.97
W_0 (mm)	0.041	0.082	0.164	0.328	0.407	0.794	1.452	2.255

The smaller setups with slightly more standardized mirrors operates far outside of the Rayleigh range. Since it is not obvious why the Herriott configuration is so successful a naive approach to advance along a horizontal line on the mirrors was attempted, instead of advancing in a circular pattern as in figure 2.12 b). In the software FRED such cavity was modelled, trying different input angles, to make the beam walk along a line on the mirrors, shown in 3.4. While this was sensitive to the incoming angle it was possible. A configuration like this is unconventional, but might provide insight in what is going on in an MPC, and why it works so well. If it is possible it might also further allow compression, as the beam size can be kept large.

In figure 3.5, a comparison between the previously implemented cells [3, 4] and the proposed set up is illustrated. There are some differences that allow the previous realization, such as the pulse duration being longer or the peak power being lower. A longer wavelength is used, which also affects the cell mode.

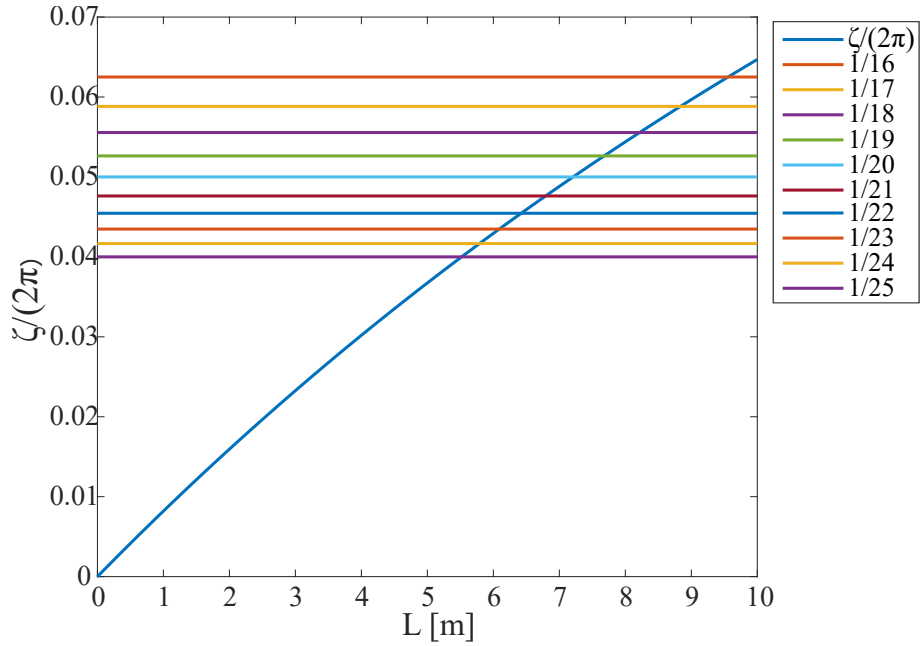


Figure 3.3: The accumulated Gouy phase during one round trip for different cavity lengths, using a defocusing mirror with radius of curvature 35 m. The lines are plotted for different fractions q/N and intersection of the phase with those lines means the re-entrant condition is fulfilled, for N round trips. With 25 round trips the cavity becomes around 5.5 m, but a more compact set up could be obtained by using more round trips, or folding the beam[4].

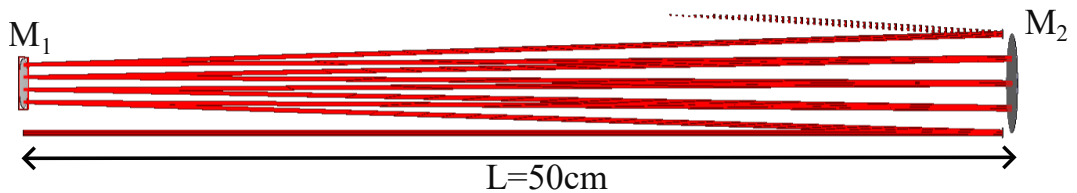


Figure 3.4: The convex-concave non-Herriott cell modelled in FRED. The cell length is 50 cm, the radius of curvature of M_1 is 0.5 m and the Radius of curvature of M_2 is -1 m.

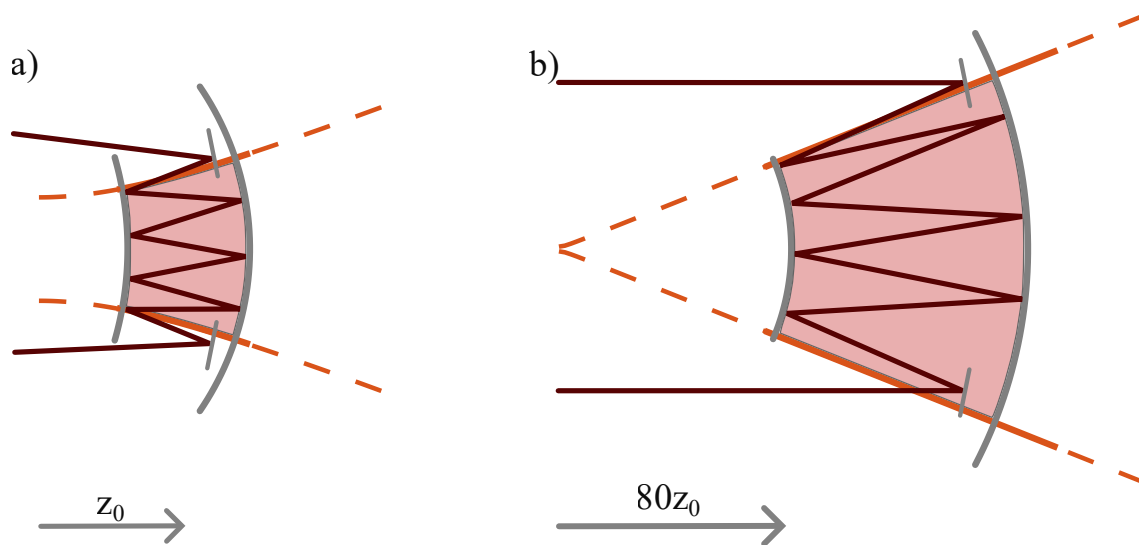


Figure 3.5: A comparison between the convex-concave MPC's implemented in [3, 4] and the chosen approach. In the previous cases the pulse power is slightly lower while the input pulse duration is much longer. The wavelength is also different which affects the scaling between beam width and wavefront radius of curvature, and a different number of round trips is used.

Chapter 4

The Experimental Set Up

4.1 The Laser Source

The Laser source is a Ti:Sapphire chirped pulse amplification laser system, used for Pump-Probe experiments such as RABBIT or KRAKEN [24]. It is operated at a repetition rate of 3 kHz, with a pulse energy up to 4 mJ, a central wavelength $\lambda_0 = 800$ nm and a tuneable spectral bandwidth of 40 nm to 80 nm [24]. In this work it was operated with a pulse energy of 3 mJ, pulse duration of 26 fs Full width half maxima (FWHM) (Fourier transform limit (FTL) of 25.2 fs) measured with a Wizzler, shown in figure 4.1 directly at the exit of the laser. In figure 4.1 b), the beam out of the laser is pictured with a false color scale to enhance contrast in the intensity structure of the beam. Below in, 4.1 d) the intensity profile of the focus is shown. The beam coming out of the laser is 28 mm in diameter, at $1/e^2$. The beam parameters are collected in table 4.1 for an overview.

Table 4.1: Laser Parameters

central wavelength λ_0	pulse duration (FWHM) τ_0	spectral bandwidth $\Delta\lambda$	Pulse energy E_p
800 nm	26 fs	70 nm	3 mJ

Assuming the beam has a Gaussian temporal shape, the peak power can be calculated as $P = 0.94E_p/\tau$, which for the above parameters becomes $P = 0.1 \times 10^{12}$ W. The intended nonlinear material, fused silica, has a linear refractive index $n_0 = 1.45$ at $\lambda = 800$ nm and a nonlinear refractive index $n_2 = 3 \times 10^{-20}$ W m⁻². Putting this into the equation for the critical power, assuming a Gaussian spatial profile, the critical power becomes $P_{cr} = 1.8962\lambda^2/(4\pi n_0 n_2) = 2.2$ MW. This is significantly lower than the laser power, and the power to critical power becomes $P/P_{cr} = 52000$ which is a very large value.

4.2 Building the MPC

Based on the previous calculations and raytracing of the MPC (see figure 3.4), a cell design was chosen and constructed in the lab. First, the beam size of the collimated input laser beam was measured, and based on this measurement a mode matching mirror was chosen.

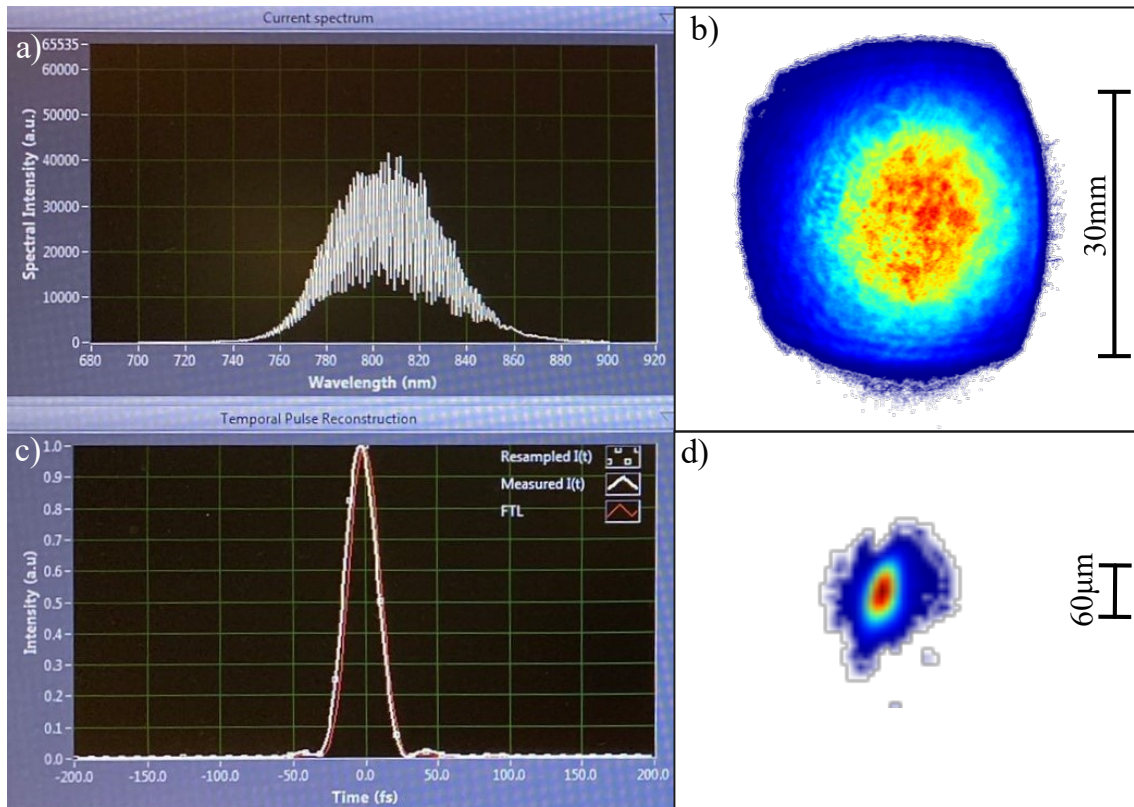


Figure 4.1: In a) the spectral interference and a reference, measured with a Wizzler [25] is shown, in c) the reconstructed pulse. Figure b) shows the a picture of the beam at the output of the laser with a false color scale to enhance contrast, and d) shows the focus of the beam in false color scale.

The cavity was aligned using mirrors $R_1 = 0.5$ m, $f_1 = -0.25$ m and $R_2 = -1$ m, $f_2 = 0.5$ m. This was done with four bounces on the defocusing mirror M_1 , and three bounces on the focusing mirror M_2 , and a cavity length of 53 cm. The beam size was measured at M_1 and M_2 . To couple out of the cavity, a flat mirror was inserted at the fourth bounce of M_2 (which was outside of the mirror). The reflected, diverging beam was sent to a focusing mirror with radius of curvature and focal length $R_{col} = 2$ m, $f_{col} = 1$ m placed 1 m from the virtual focus resulting in a collimated beam.

Before placing the glass plate, anti reflection coated fused silica, the transmission of the cell was measured by comparing the input power to the output power. Once the glass plate was placed and properly aligned this was repeated. The aligned cell is shown in figure 4.2.

The spectral broadening was measured with a spectrometer, and compared to the input spectrum measured with the same spectrometer before the cell. Spectra were collected for several positions of the glass plate in the cell, and for the optimized position, a spectrum for twice the amount of nonlinear medium was obtained. The focus of the input beam was imaged, and a few additional pictures were saved at distances 2 cm, 3 cm and 4 cm from the geometrical focus, to be used in the Gerchberg-Saxton(GS) algorithm, which retrieves phase information based on intensity measurements in two planes [26]. The same was done for the output beam, with 0 mm, 1 mm and 2 mm of fused silica in the cell. The reconstructed phase can then be used to simulate the beam as it propagates or to calculate the M^2 of the

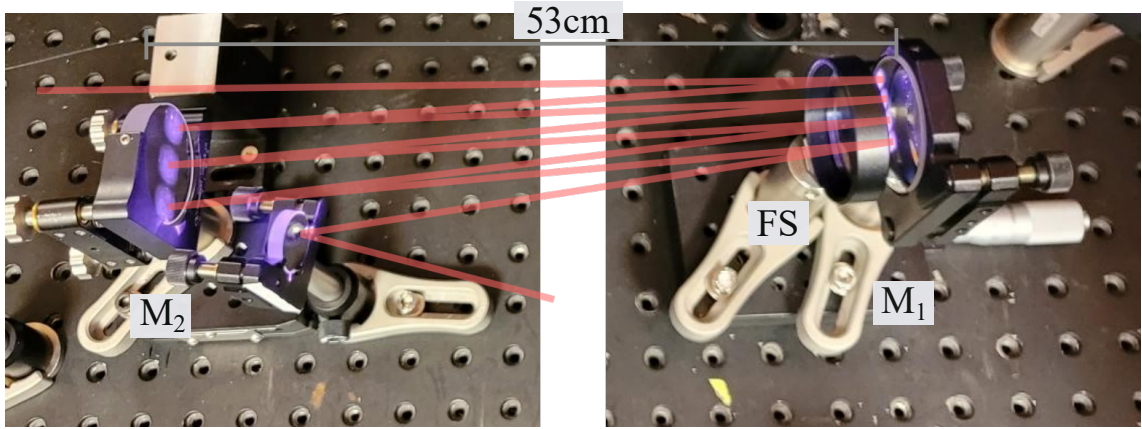


Figure 4.2: Aligned MPC. To the left is the focusing mirror, in front of it the out-coupling mirror and to the right the glassplate and defocusing mirror. Mode matching mirror is not included but could be found further to the left. The figure is cropped with the centre cut out for illustrative purposes.

beam.

The temporal behaviour of the output pulse was measured using Frequency-resolved Optical Gating (FROG). FROG can retrieve the pulse in the time domain by recording the spectrally resolved auto correlation trace [27]. The measurement was done with and without the glass plate, for different input durations. The different input durations were obtained by chirping the output pulse of the laser. The FROG measurement was done both with the uncompressed output pulse, and with the resulting pulse after reflection on two chirped mirrors with GDD -250 fs^2 , each.

4.3 Characterization of the Convex-Concave MPC

In this section, the result of the characterization measurements performed on the MPC in the lab will be presented.

The power transmission was measured to 81%. The cavity mirrors are silver mirrors with a reflectivity of 98% and in total there are 12 bounces, including 7 bounces in the cavity and one bounce on each remaining mirror. A quick calculation $0.98^{12} = 0.785$ which is in agreement with the practical result. Note that not all of the mirrors are silver mirrors, but rather dielectric with a slightly higher reflectivity. When the glass plate is inserted the efficiency did not change noticeably, pointing towards little to no losses by reflection or absorption in the anti-reflection coated glass-plate.

A photograph was taken of the incoming beam, and of the out coming beam using 1 mm and 2 mm of fused silica, presented in figure 4.3 a), b) and c). While input and output look different from each other neither is free from spatial structure. Comparing 4.3 b) and c) the contrast between different spatial structures appears more diffuse in b) than in c). The structures present in c) remind of an enhanced version of the ones in b), which could be the case due to small scale self focusing in the glass plates. As the beam power is several thousand times the critical power, some self focusing effect is to be expected.

When measuring and reconstructing the input beam with the GS-algorithm, the M^2 values of the input beam is around 2 while for the output beam the M^2

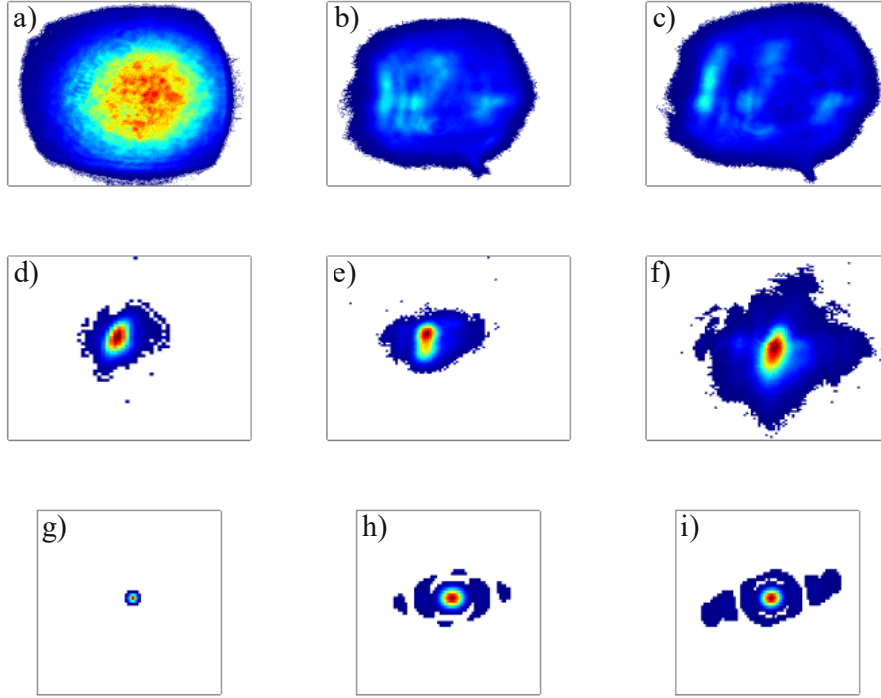


Figure 4.3: The top row shows photographs of a) input beam, b) output beam using 1 mm fused silica, c) output beam using 2 mm fused silica, all in the far field. The middle row shows in the same order d) input, e) output 1 mm fused silica, f) output 2 mm fused silica, all in the focus. The bottom row g-h) is the two dimensional Fourier transform of the far field beams.

is very different depending on what input planes are used (ranging from 2.5 to 4). It is likely that the beam is so strongly aberrated that the algorithm becomes less effective. When decomposing into Zernike-polynomials it is clear that there is a lot of astigmatism present, but also other orders are strong in the output beam. The same decomposition for the input beam shows primarily astigmatism.

Even if the M^2 values are not ideal for the output beam, there are applications where the M^2 is not as important as the intensity of the focus. The focus of the input and output beams are shown in figure 4.3 d), e) and f). In d) the input focus is shown, and in e) and f) the output focus when using 1 mm and 2 mm of fused silica. There is a difference between e) and f) in the number of filters used, and in f) there seems to be a wing like structure that is not visible in e). To further improve the output, the angles inside the cavity could be minimized. There is also a small clipping as the beam couples out, which induces some fringes.

To better quantify the growth of structure the intensity profiles of the collimated beams were Fourier transformed. The result is shown in figure 4.3 g), h) and i). The input beam is in the Fourier plane very round, indicating that the overall angular structure is well behaved. The two output beams are round, but display additional structures in the Fourier domain. In both cases there are horizontal wings present, but they appear stronger in i), indicating that it is related to the nonlinear medium.

There also appear to be a ring like structure surrounding the central spot, which is not completely connected in h), but appears to have grown in i). While the two transforms h) & i) are different, they still share similarities. The increased k_{\perp} structure is most likely a result of small scale self focusing.

If a comparison between the displayed images and that of the transmitted beam without any nonlinear medium inserted were made it could further imply whether this structure comes from the cavity and is enhanced by the nonlinear material. Mécahin et al. found in 2004, both experimentally and numerically that self focusing of astigmatic beams at high power cause the beam to break up into two filaments [28]. If this is something that is due to the present astigmatism, it might be possible to combat by using a deformable mirror, where the pattern could be changed by deforming the mirror to allow compensation of astigmatism at each bounce.

Already at the input the beam is astigmatic, and after passing through the MPC without correcting, the beam was so astigmatic that the vertical and horizontal focuses were completely separated. Considering that the beam makes nine bounces on spherical surfaces with a non-zero angle of incidence this astigmatism is not surprising, and one benefit of the Herriott cell becomes very apparent. As astigmatism arises when a beam is (de)focused at an angle, it increases as it passes through the cell. In a Herriott cell the beam bounces in a circular pattern, introducing equally much astigmatism in the vertical and horizontal planes, and therefore compensating.

To minimize the astigmatism of the output beam the collimating mirror after the cavity was angled downward to introduce astigmatism vertically, and after some optimization the astigmatism was significantly reduced, and the result is presented in figure 4.3 e) and f).

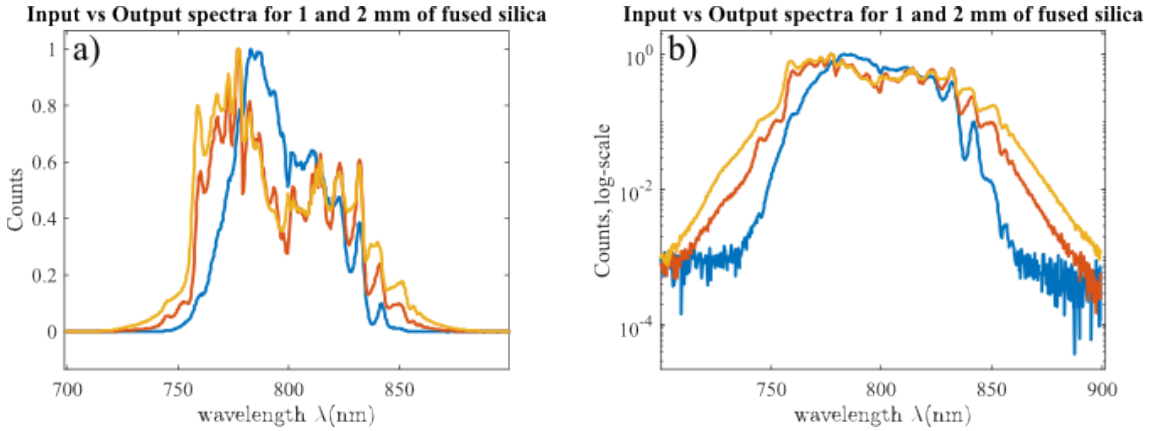


Figure 4.4: Comparison between input (blue), output spectra with 1 mm fused silica (red) and output spectra with 2 mm fused silica (yellow). In a) plotted with a linear scale and in b) plotted with a logarithmic y-axis.

The measured input and output spectra is presented in figure 4.4 normalized and with linear (a) and logarithmic (b) scale. The output spectra were measured with insertion of both 1 mm and 2 mm fused silica (red and yellow). Considering spectral widths, the FWHM $\Delta\lambda_{FWHM}$ increases from 50 nm to 80 nm, while $\Delta\lambda_{1/e^2}$ increases from 80 nm to 100 nm and 110 nm. For pulse compression often the wings, not contained in the mentioned widths, play a role. The input spectral signal starts around 745 nm and ends around 855 nm, giving a $\Delta\lambda$ of 110 nm. For the broadened spectra the corresponding values are 730 nm and 720 nm to 875 nm and 880 nm giving

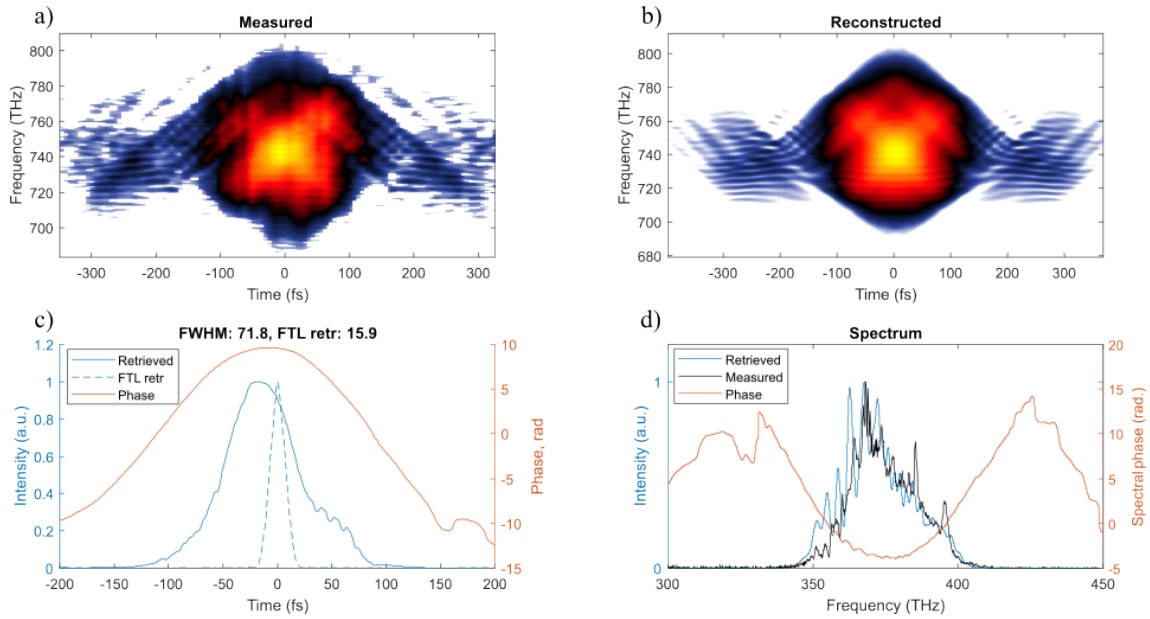


Figure 4.5: The result and reconstruction of the FROG measurement. In a) the resulting measurement is shown, and in b) is the reconstruction. In c) the temporal profile of the pulse is shown. The FWHM pulse duration is 71.8 fs with a reconstructed Fourier limit of 15.9. In d) the measured spectra and a reconstructed spectra is shown with the spectral phase. The behaviour of the spectral phase is that of a parabola.

$\Delta\lambda$ of 145 nm and 160 nm, read from figure 4.4 a).

The broadened spectra have undergone reshaping, characteristic of Self Phase Modulation. The reshaping look quite similar for the two thicknesses. It could be of interest to control the output spectral shape, which inspires the question of how the broadening depends on input spectral shape.

The result of the performed FROG measurement using a Fourier limited input pulse is presented in figure 4.5, along with a reconstruction of the measurement. In 4.5 c) the spectral phase looks very similar to a parabola, although with some small ripples. Such phase corresponds mainly to 2nd order dispersion. The pulse duration is measured to 71.8 fs. In figure 4.6 the same measurement is performed, but before entering the FROG scheme the pulse is compressed by two bounces on chirped mirrors. As can be seen in the figure, the pulse is compressed to 19.2 fs and Fourier limited as 14.9 fs which corresponds to a temporal compression ratio of $K = \frac{26 \text{ fs}}{19.2 \text{ fs}} = 1.35$. The compression was performed with mirrors available from an earlier experiment, and could be improved with more effort. Using a FTL of 15 fs instead of the FWHM yields $K = 1.73$. The difference in Fourier limit between the two measurements is 1 fs, which is a reasonable agreement taking into account that the FTL is calculated from the retrieved spectrum.

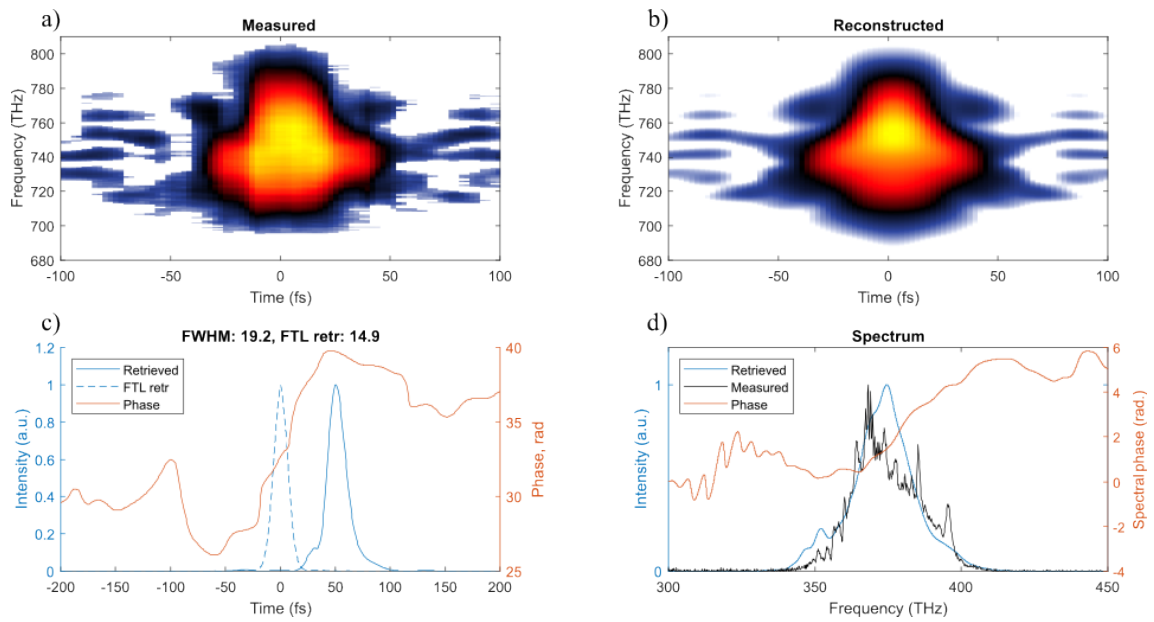


Figure 4.6: The result and reconstruction of the FROG measurement after letting the beam bounce on 2 chirped mirrors (250 fs^2). In a) the resulting measurement is shown, and in b) is the reconstruction. In c) the temporal profile of the pulse is shown. The FWHM pulse duration is 19.2 fs with a reconstructed Fourier limit of 14.9 fs. In d) the measured spectra and a reconstructed spectra is shown with the spectral phase.

Chapter 5

Simulations

In this section a description of the performed simulations will be provided. First a solver for the time-independent nonlinear Schrödinger equation will be described, along with the tests performed to verify the solver. Second the code simulating an MPC will be described, along with some performed simulations and the result thereof.

The goal of this part of the project was to create a simulation tool to study the spatial properties and beam evolution of a beam propagating in an MPC, especially due to self focusing effects. Such tool would provide insight in how the MPC behaves.

To perform those simulations, several tools were required. First, a Fourier propagator to simulate diffraction was implemented. This was then used to implement a solver for the nonlinear Schrödinger Equation for a beam propagating in a nonlinear material. A focusing element was described by applying curvature to the input beam, and to simulate an MPC all three codes were put together. Finally, there are no perfect Gaussian beams, and a tool to generate realistic beams was implemented.

First the Fourier Propagator will be described, then the solver for the nonlinear propagation with verification and then the MPC code and some result. Finally the tool for generating realistic beams will be introduced, along with some examples.

5.1 Fourier Propagator

In the code, the transverse complex amplitude of a beam U is represented by a two dimensional matrix, $m \times m$. This is propagated by taking it to the Fourier domain, which corresponds to decomposing it into plane waves, each with an angular wavenumber $k_i, i = x, y$. In the Fourier domain, the different components are multiplied by the transfer function of free space, and transformed back to real space (x, y) . The equations are as follows;

$$U(x, y)|_{z=0} \text{ inserted into the propagation tool} \quad (5.1)$$

$$U(x, y)|_{z=0} \xrightarrow{\mathcal{F}} \mathcal{U}(k_x, k_y) \quad (5.2)$$

$$\mathcal{U}(k_x, k_y) \cdot \exp\left(ik\sqrt{1 - \frac{k_x^2 + k_y^2}{k^2}}\right) = \mathcal{G}(k_x, k_y) \quad (5.3)$$

$$\mathcal{G}(k_x, k_y) \xrightarrow{\mathcal{F}^{-1}} U(x, y)|_{z=d} \quad (5.4)$$

and $U(x, y)$ have been propagated from $z = 0$ to $z = d$. \mathcal{G} is the Fourier transform of $U(x, y)$ in the output plane $z = d$ the same way as \mathcal{F} is the Fourier transform of

$U(x, y)$ in the input plane $z = 0$.

This was tested by propagating a Gaussian Beam a distance d using the implemented tool, and comparing it to the same Gaussian beam propagated analytically.

5.2 Solving the Nonlinear Schrödinger Equation

The nonlinear Schrödinger equation, presented in section 2.4.2 equation 2.44, is a nonlinear differential equation that has no analytical solution. Numerical solutions can be obtained by applying appropriate numerical method. There are several possibilities to chose from, but in this work, a split step Fourier method was chosen. For a small step the equation can be split into a linear part and a nonlinear part. The script solves the Non-Linear Schrödinger Equation by the Split Step Fourier Method resulting in the acronym NLSE-SSFM.

The linear part represents linear propagation in free space, and looks like the regular wave equation. Taking a step h in the propagation direction with the linear part describes diffraction. This can be solved using the Fourier propagator previously implemented. This is contained in the name, the Split step Fourier method, as the problem is first split in to two problems, and then one of those problems is solved in the Fourier domain.

Solving the nonlinear part is done by using the Runge Kutta 4th order (RK4) scheme [29]. The problem is evaluated at four positions in the step, generating four slopes. At each step h a weighted sum of them is taken, multiplied by the sep size h and added to the initial value of the step. When solving the nonlinear step the result of the linear step is used as an input.

The equation to solve is the nonlinear Schrödinger equation;

$$\frac{\partial A}{\partial z} = -\frac{j}{2k}\nabla_{\perp}^2 A - \frac{jk n_2}{2}|A|^2 A \quad (5.5)$$

and for simplicity operator notation is used to obtain

$$-\frac{j}{2k}\nabla_{\perp}^2 = \hat{D}, \quad \frac{jk n_2}{2}|A|^2 = \hat{N} \quad (5.6)$$

$$\frac{\partial A}{\partial z} = -(\hat{D} + \hat{N})A \quad (5.7)$$

Propagating a beam a distance d in a nonlinear material is the same as solving this equation using the input beam as an initial value. By taking small steps along the propagation direction the problem can be split, and the equation can be solved as follows:

$$A(x, y)|_{z+h} = \exp(h\hat{N}) \exp(h\hat{D})A(x, y)|_z \quad (5.8)$$

which is done by solving the linear operator in the Fourier Domain, as described in the previous section, and evaluating the nonlinear operator in real space with an RK4 scheme, using the solution of the linear step as an initial value;

$$A(x, y)|_{l_s} = \mathcal{F}^{-1}(H(k_x, k_y) \cdot \mathcal{F}(U(x, y))) \quad (5.9)$$

$$A(x, y)|_{z+h} = RK4(\hat{N})A(x, y)|_{l_s}. \quad (5.10)$$

$H(k_x, k_y)$ is the transfer function of free space, as in equation 5.3.

When both linear and nonlinear propagation steps have been performed the beam has been propagated a small step h . This is then done again and again, until the accumulated distance is equal to the propagation length in the nonlinear medium.

The step h needs to be small enough to allow separation of the problem, but large enough as to not make the problem unnecessary time consuming. To satisfy this the step is made adaptive, by limiting the maximum amount of nonlinear phase that can be accumulated at a step. If the intensity is large, the nonlinearity increases and to limit the nonlinear phase a smaller step is taken. This decreases the time consumption and increases resolution. One benefit of taking the Fourier transform of the linear step is that the linear evaluation becomes exact.

5.2.1 Verification of the NLSE-SSFM

To verify the solver Gaussian beams of varying power were propagated through a nonlinear medium and compared to results of previous work, mainly by Marburger [11, 16]. In figure 5.1 the on axis intensity of a Gaussian beam is shown as it propagates through a nonlinear material, entering at the waist.

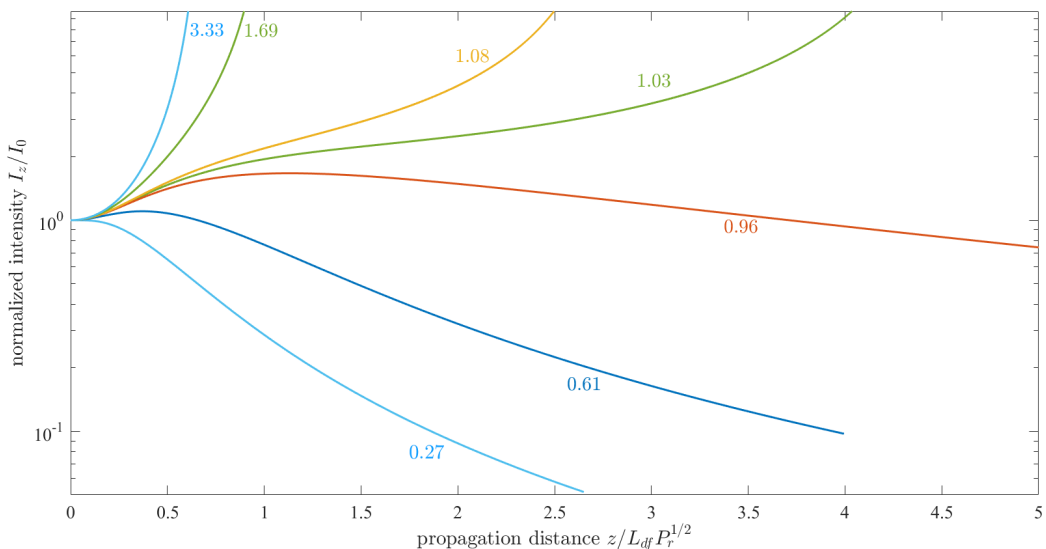


Figure 5.1: On axis intensity evolution for different powers. The input beam is a Gaussian beam at the waist. At power to critical Power ratios of less than one the input beam undergoes a spatial reshaping, as it evolves into a Townes profile instead of a Gaussian profile. The same process occurs also for powers that are close to, but larger than, the critical power, where the beam first reshapes to a profile similar to the eigenmode. It then propagates with a smaller intensity increase, to finally self focus rapidly. For higher powers this behaviour stops, and the beam self focuses right away. The result is very similar to that in reference [16].

The result is obtained by propagating a Gaussian beam of different powers to critical power ratios, P/P_{cr} displayed in the figure beside each graph, in a nonlinear material. The beam can continue diverging, or self focus and then continue diverging, or self focus until collapse, depending on if it carries a sufficient power. For P/P_{cr} -ratios below 1 but above 0.27 the beam first self focuses but then continues

diverging. This is shown by the initial increase of the on axis intensity, but as the beam propagates the on axis intensity starts decreasing again. If the P/P_{cr} -ratio is slightly above 1 (1.03 and 1.08 in the figure) the curve shows the same initial increase, then the intensity increase is halted, until it again starts increasing exponentially. In both of the cases, the initial increase is due to a reshaping of the Gaussian beam, where the initially Gaussian profile is altered towards a Townes profile. For the higher P/P_{cr} -ratios the on axis increase is very rapid, and shows no plateau. The reshaping has no time to occur but the dynamics goes directly towards collapse.

5.2.2 Simulating the MPC

As previously described the beam needs to be mode matched to the cavity. Once it is mode matched it can be propagated to some place within the MPC, where it can be inserted.

The beam is now inserted into the MPC. It is propagated via Fourier Propagation to the Nonlinear medium. In the nonlinear medium it is propagated using the nonlinear propagator, (NLSESSFM). Next it is propagated to the first cavity mirror, where it is re-(de-)focused. The same path is propagated but backwards, and on the second cavity mirror the beam is re-focused and the transverse intensity profile of the beam is plotted. A schematic of this is shown in 5.2.

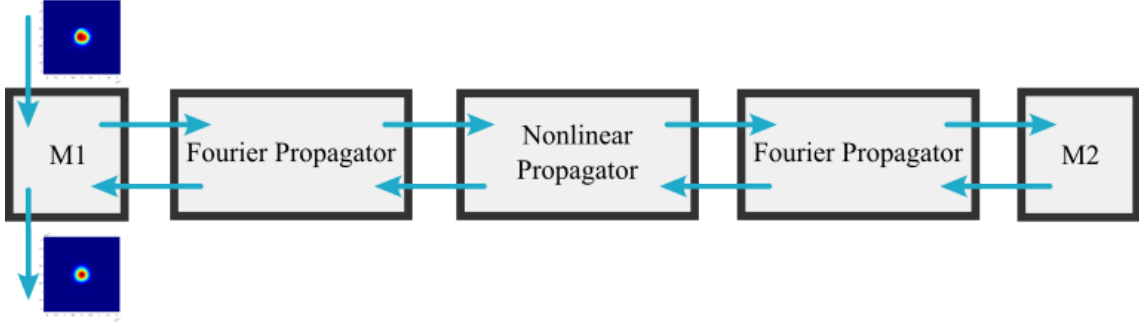


Figure 5.2: A schematic pseudo code representation of the simulation of an MPC.

This can be described mathematically, using $z = z_2$ for the plane with the focusing mirror, $z = z_1$ for the plane with the defocusing mirror (though it also works for a focusing mirror), $z = z_{NL,in/out}$ for the plane of the nonlinear medium and L_{NL} for the length of the nonlinear medium.

$$A(x, y)|_{z_{NL,in}} = \mathcal{F}^{-1}(H(k_x, k_y, d_2)\mathcal{F}(A(x, y)|_{z_2})) \quad (5.11)$$

$$A(x, y)|_{z_{NL,out}} = \mathcal{N}(A(x, y)|_{z_{NL,in}}) \quad (5.12)$$

$$A(x, y)|_{z_1} = \mathcal{F}^{-1}(H(k_x, k_y, d_1)\mathcal{F}(A(x, y)|_{z_{NL,out}})) \quad (5.13)$$

$$A(x, y)|_{z_1} = h_{dfm}A(x, y)|_{z_1} \quad (5.14)$$

$$A(x, y)|_{z_{NL,in}} = \mathcal{F}^{-1}(H(k_x, k_y, d_1)\mathcal{F}(A(x, y)|_{z_1})) \quad (5.15)$$

$$A(x, y)|_{z_{NL,out}} = \mathcal{N}(A(x, y)|_{z_{NL,in}}) \quad (5.16)$$

$$A(x, y)|_{z_2} = \mathcal{F}^{-1}(H(k_x, k_y, d_2)\mathcal{F}(A(x, y)|_{z_{NL,out}})) \quad (5.17)$$

$$A(x, y)|_{z_2} = h_{fm}A(x, y)|_{z_2} \quad (5.18)$$

where $H(k_x, k_y, d_i)$ is the transfer function of free space to propagate distance d_i , and d_i is the distance between the nonlinear medium and mirror i . \mathcal{N} is the nonlinear solver as previously described, and $h_{dfm}, (h_{fm})$ is the impulse function of the defocusing, (focusing), mirror, defined $\exp(jk(x^2 + y^2)/(2f))$ where f is the focal length of the mirror.

First the code was verified by simulating a cavity close to the focus. The aim is to go further away from the focus. As the beam propagates away from the focus, it grows. Eventually it will hit the edge of the numerical window. When this happens the beam folds back - much like aliasing. This no longer describes propagation, and therefore the window size needs to be increased so that the beam can fit within.

When the beam is defined in the far field it's width is W_L . The width in the focus is related to this by $W_0 = \frac{f\lambda}{\pi W_L}$ where f is the focal length of a lens. The convergence of the focused beam is given by $\theta = W_L/f$. This needs to be sampled well, and therefore it is over-sampled by π so that $\theta_{max} = \pi W_L/f$. The maximum transverse k then becomes $k_{\perp, max} = 2\pi \sin(\theta_{max}/\lambda) = 1/2(\Delta x)$ which relates to the spatial resolution in the focus, $\Delta x \approx \lambda/(4\pi\theta_{max})$ obtained using small angle approximation. This gives a required resolution, and the window is found by taking the number of points m multiplied with the pixel size Δx , $OP = m\Delta x$.

Setting the optical window to $OW = 2\pi W_2$ the number of additional points required to resolve the problem can be obtained, as $OW/(\Delta x) = m_2$. This keeps the k -transverse window, as that is dependent on Δx as $2k_{max} = 1/\Delta x$, but it also makes the grid finer.

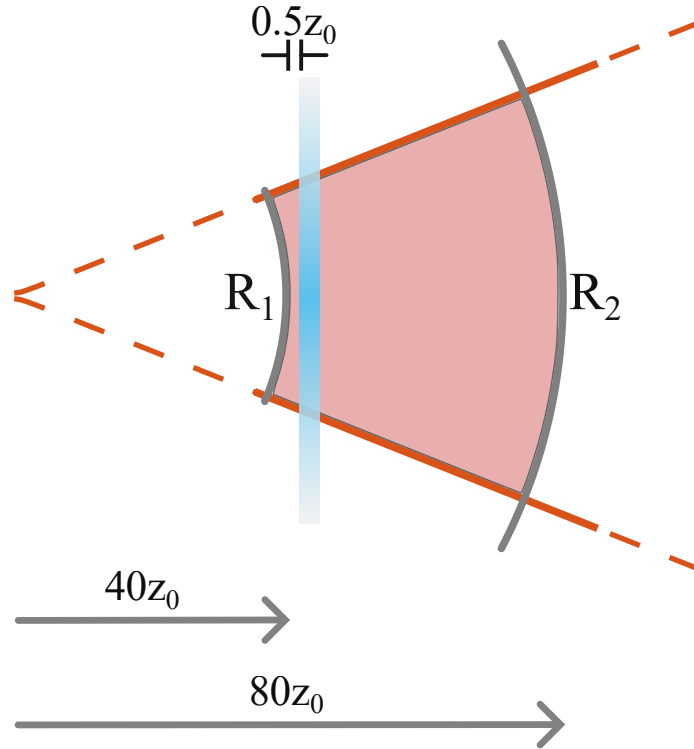


Figure 5.3: The setup used in the simulations. The focusing mirror is placed at $z_2 = 80z_0$ from the focus, with a Radius of curvature $R_2 = 80z_0(1 + (z_0/(80z_0))^2) \approx 80z_0$. The defocusing mirror is placed at $z_1 = 40z_0$ with radius of curvature $R_1 \approx 40z_0$. The nonlinear medium is 1 mm thick and placed at $0.5z_0$ from the defocusing mirror.

This allowed simulation of the physical cavity, with the focusing mirror placed at $80z_0$ and the defocusing mirror placed at $40z_0$. A schematic of the simulated set up is shown in figure 5.3. An initial test was done propagating a Gaussian beam in the cavity with no nonlinear medium inserted, shown in figure 5.4, and then beams of different powers were propagated in the cavity.

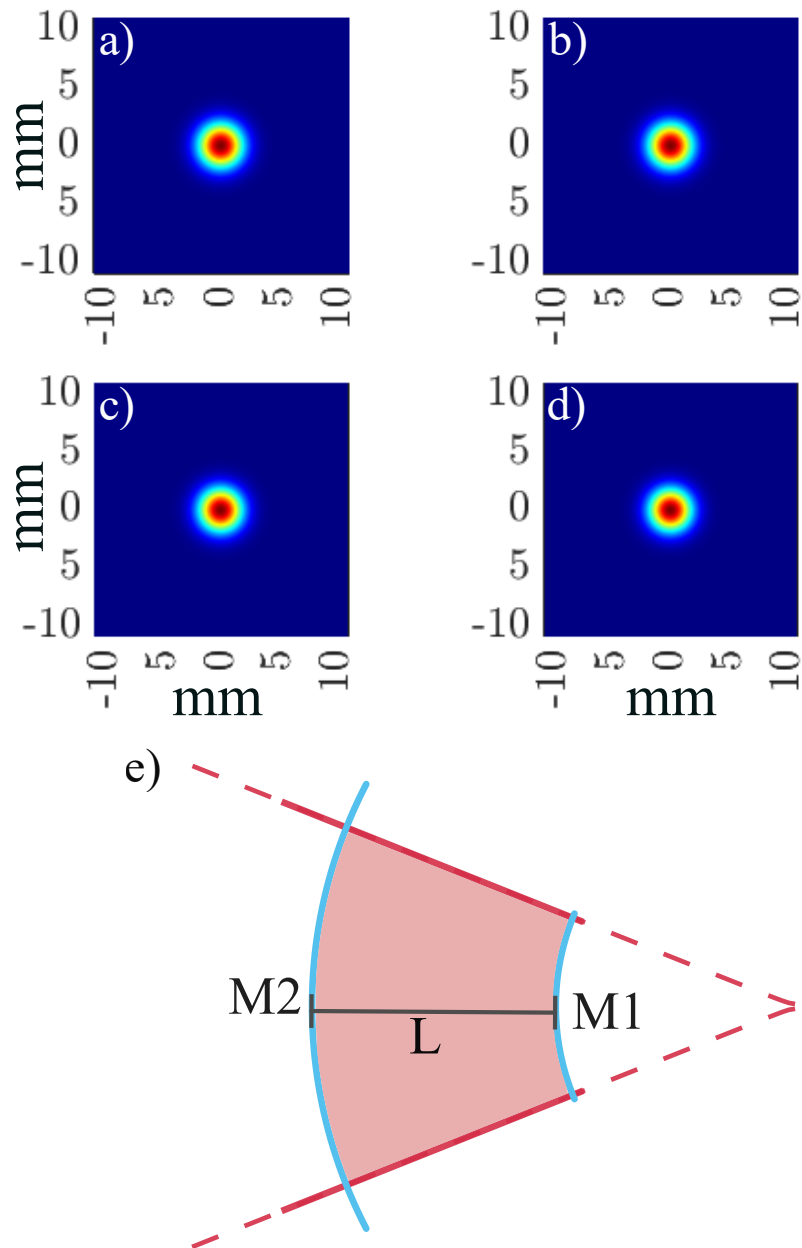


Figure 5.4: A Gaussian beam at the focusing mirror in an MPC sketched in figure 5.3, and in e. a (b,c,d) shows the beam on the focusing mirror after the 1st(2nd, 3rd, 4th) round trip.

Figure 5.4 shows that a Gaussian beam that has been mode matched to the cell retraces itself each round trip. This is used as a verification that propagation in the cavity behaves as expected, and as a reference when glass is inserted.

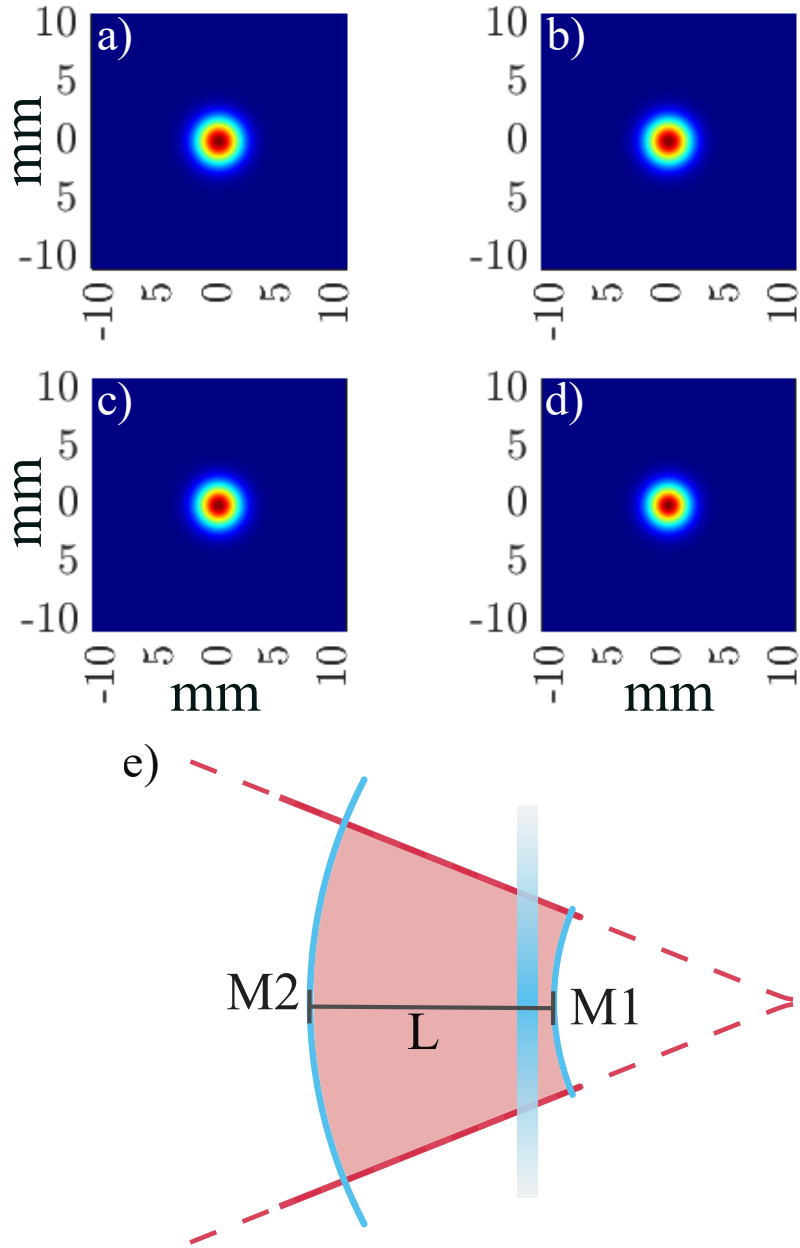


Figure 5.5: A Gaussian beam with P/P_{cr} ratio of 100, at the focusing mirror in an MPC sketched in figure 5.3. a (b,c,d) shows the beam on the focusing mirror after the 1st(2nd, 3rd, 4th) round trip. The effect is very faint, but the beam width is a little smaller after each round trip.

In figure 5.5 a Gaussian beam containing 100 times the critical power is propagated through the cavity in figure 5.3. After each round trip the beam width at the second mirror has decreased. The effect is weak, but likely the intensity is strong enough to induce self focusing. This pushes the virtual focus closer to the defocusing mirror, and the beam is not properly mode matched in the cavity anymore. At this power the effect is very small. When the nonlinear medium changes the mode in the cell, in practise nonlinear mode matching should be introduced, where the self focusing in the nonlinear medium is used when calculating the cell mode [30, 31]. In

this work this has not been implemented.

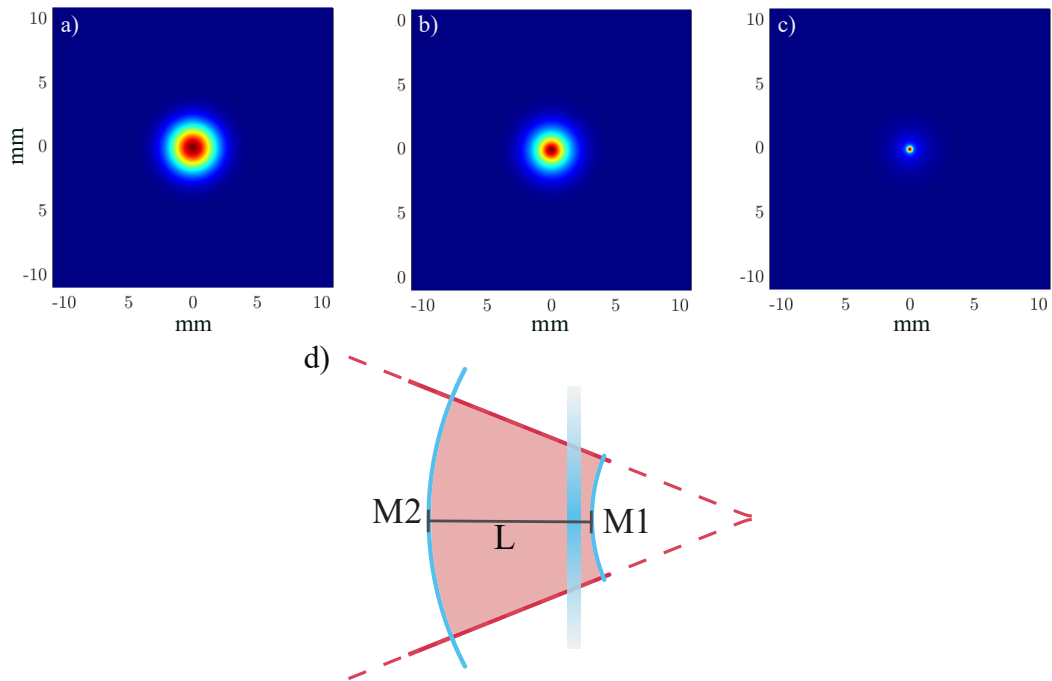


Figure 5.6: A Gaussian beam with P/P_{cr} ratio of 3 300, at the focusing mirror in an MPC sketched in figure 5.3. a (b,c) shows the beam on the focusing mirror after the 1st(2nd, 3rd) round trip. The beam is clearly smaller after each round trip. This implies a need for nonlinear mode-matching.

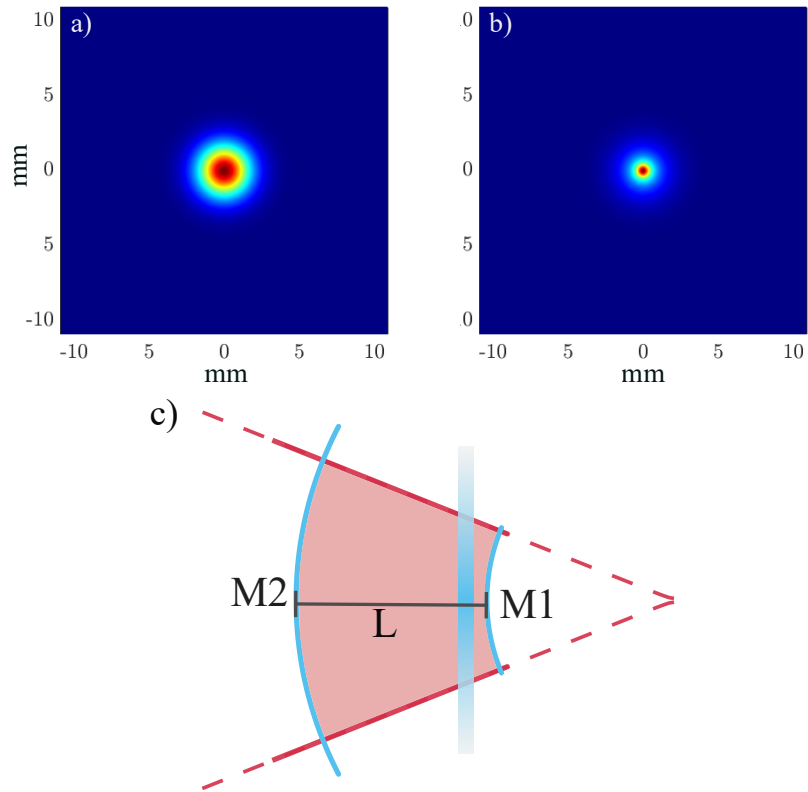


Figure 5.7: A Gaussian beam with P/P_{cr} ratio of 6 500, at the focusing mirror in an MPC sketched in figure 5.3. a (b) shows the beam on the focusing mirror after the 1st(2nd) round trip. The beam is clearly smaller after each round trip. This implies a need for nonlinear mode-matching.

5.3 Realistic Beams

While the Gaussian beam is a common approximation, in reality the beam profiles are only approximated as Gaussian beams. Self focusing is dependent on the beam profile, as is small scale self focusing, and both may cause beam degradation. It is therefore of interest to be able to simulate this in some realistic beams. While some beam profiles, such as the vortex beam or a super Gaussian can be obtained by multiplying with an angular phase or altering the Gaussian in the definition, this does not describe aberrations that may be present in realistic beams.

To model realistic beams the Zernike Polynomials are introduced. Similar to how a beam can be decomposed into plane waves, the phase of a realistic beam can be decomposed into Zernike polynomials [32, 33]. The polynomials form an orthogonal basis, where some basis functions correspond to specific aberrations, such as astigmatism or coma. By applying a set of Zernike polynomials with random coefficients within a given range a realistic beam profile can be simulated, such beam is shown in figure 5.8 a) at the input plane of the simulated MPC and in b) at the focus.

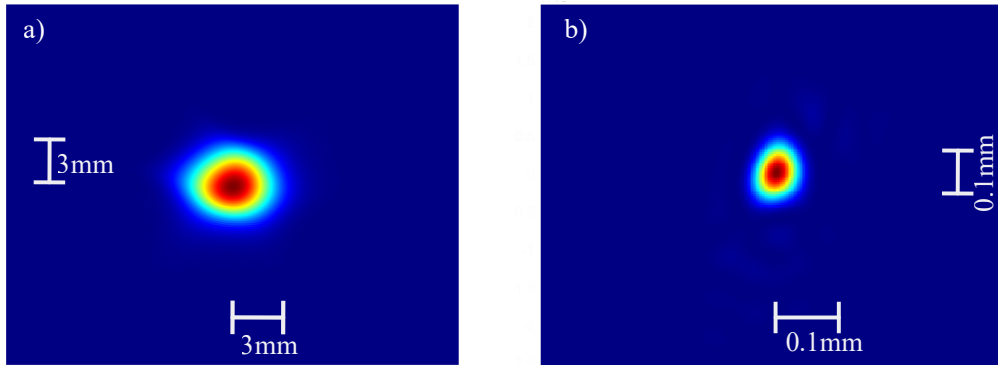


Figure 5.8: Aberrated beam at the input of the MPC (a) and the focus of the same beam(b).

First the Zernike Polynomials were applied in the far field and the aberrated beam was propagated to the focus (figure 5.8 b), as described above. Also described above, it was taken to the position of the focusing mirror where it was inserted into the cavity.

The same cavity as in figure 5.3 was used for the randomly aberrated beam in figure 5.8. This was first propagated in an empty cavity, without any nonlinear medium to be used as a reference (figure 5.9), then the power was increased to study self focusing (figures 5.10, 5.11, 5.12). The cavity is mode matched to a Gaussian beam, which has parabolic wave-fronts, but due to the aberrations this is no longer the case for the realistic beam. This is also clear in figure 5.9 where the beam clearly evolves during each round trip.

For low input powers the self focusing is not sufficiently strong to have a visible impact on the beam propagating in the cavity with a nonlinear material inserted as in figure 5.3. At a power of $200P_{cr}$ the beam evolves as in figure 5.10, and when comparing this to the empty cavity there seems to be some self focusing present, as the beam at each round trip in the different cases looks slightly different.

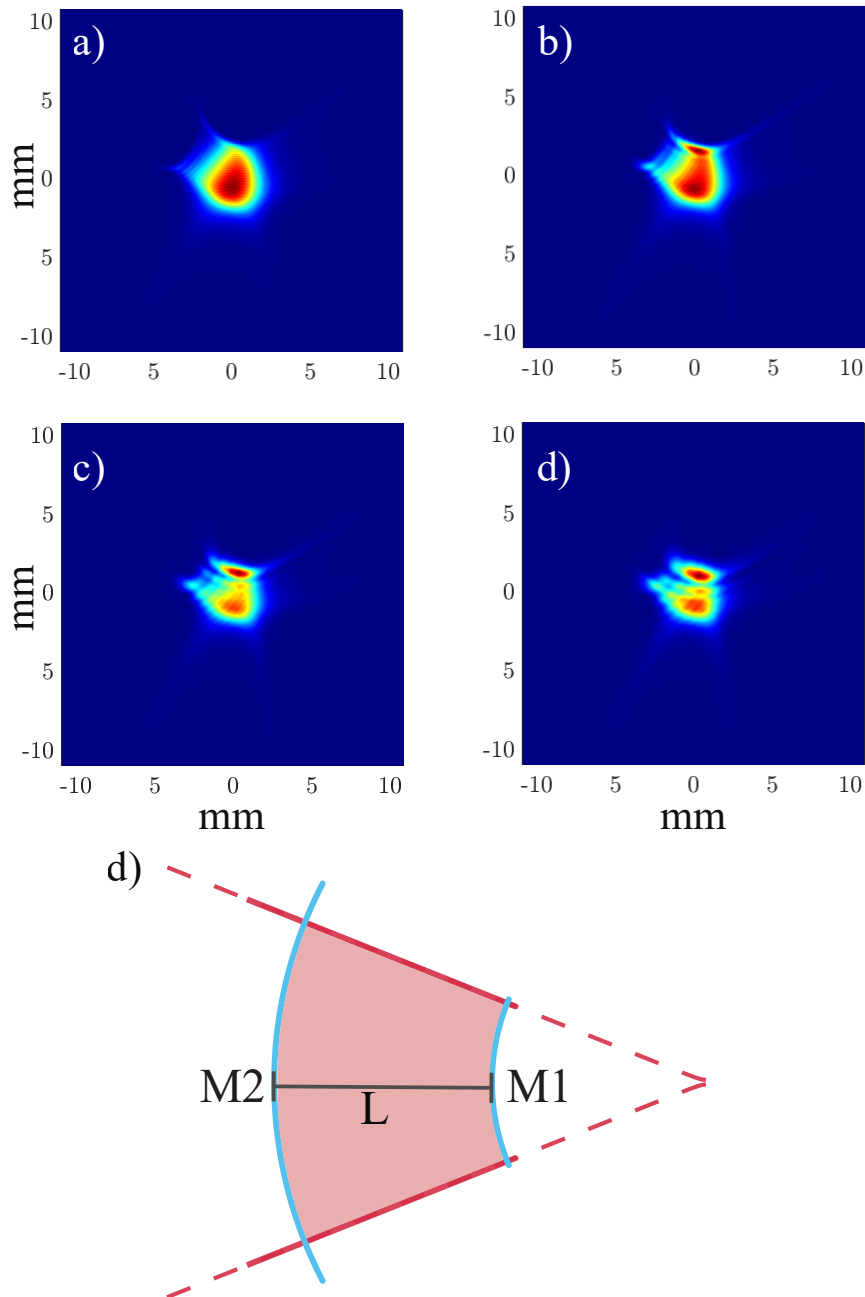


Figure 5.9: An aberrated beam in the input plane after propagating a round-trip in the cavity depicted in figure 5.3, but without the nonlinear medium inserted. a) (b,c,d) shows the 1st(2nd, 3rd, 4th) round trip. The shape is changed every round trip, as the beam is not perfectly mode matched to the cavity, because of the present aberrations altering the wave-front.

When the beam power is increased the difference to the empty cavity also grows, which is expected. The intensity increase causes the beam to self focus, as if it had been propagated through a lens. At some point the lensing becomes sufficiently strong to remarkably change the mode of the beam. This means the beam RoC at the second mirror is less than the RoC of the mirror, and the mirror can not defocus it back into itself. As mentioned previously this effect can be combated by nonlinear mode matching, as done in [30, 31].

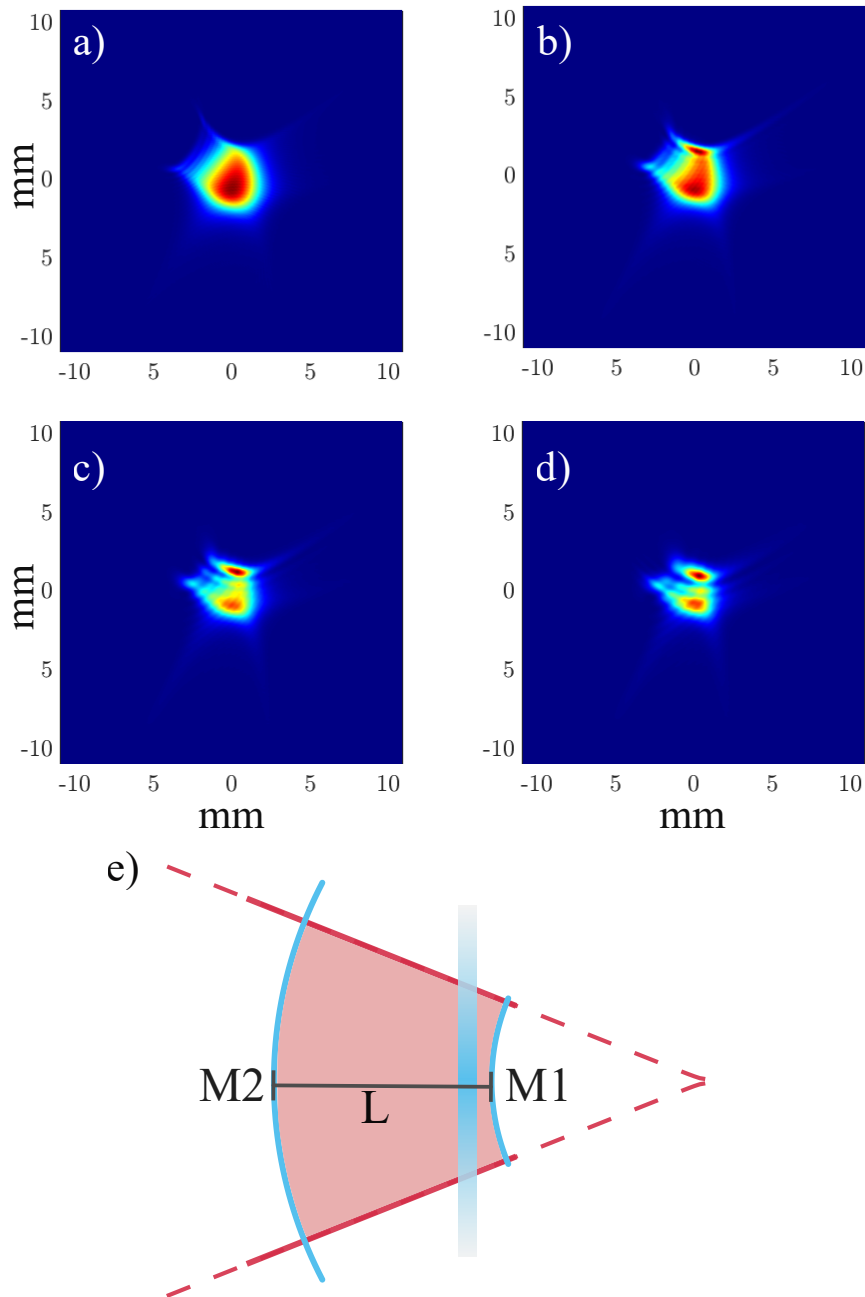


Figure 5.10: An aberrated beam with P/P_{cr} ratio of 200 in the input plane after propagating a round-trip in the cavity depicted in figure 5.3. a) (b,c,d) shows the 1st (2nd, 3rd, 4th) round trip. The shape is changed every round trip, as the beam is not perfectly mode matched to the cavity, because of the present aberrations altering the wave-front, but the beam is also undergoing some self focusing.

As the power is increased there seem to be large scale self focusing occurring, but the beam also seems to undergo some small scale self focusing. The structures formed in round trips 2, 3 and 4 (b,c and d) in figure 5.9 and 5.10 appear also in figure 5.11 and 5.12 but with hot spots. The beam seems to be diffracting as it propagates in the cavity, and this could lead to high intensities seeding the beam break-up.

The simulated cavity is matched for the same mode as the physical cavity in

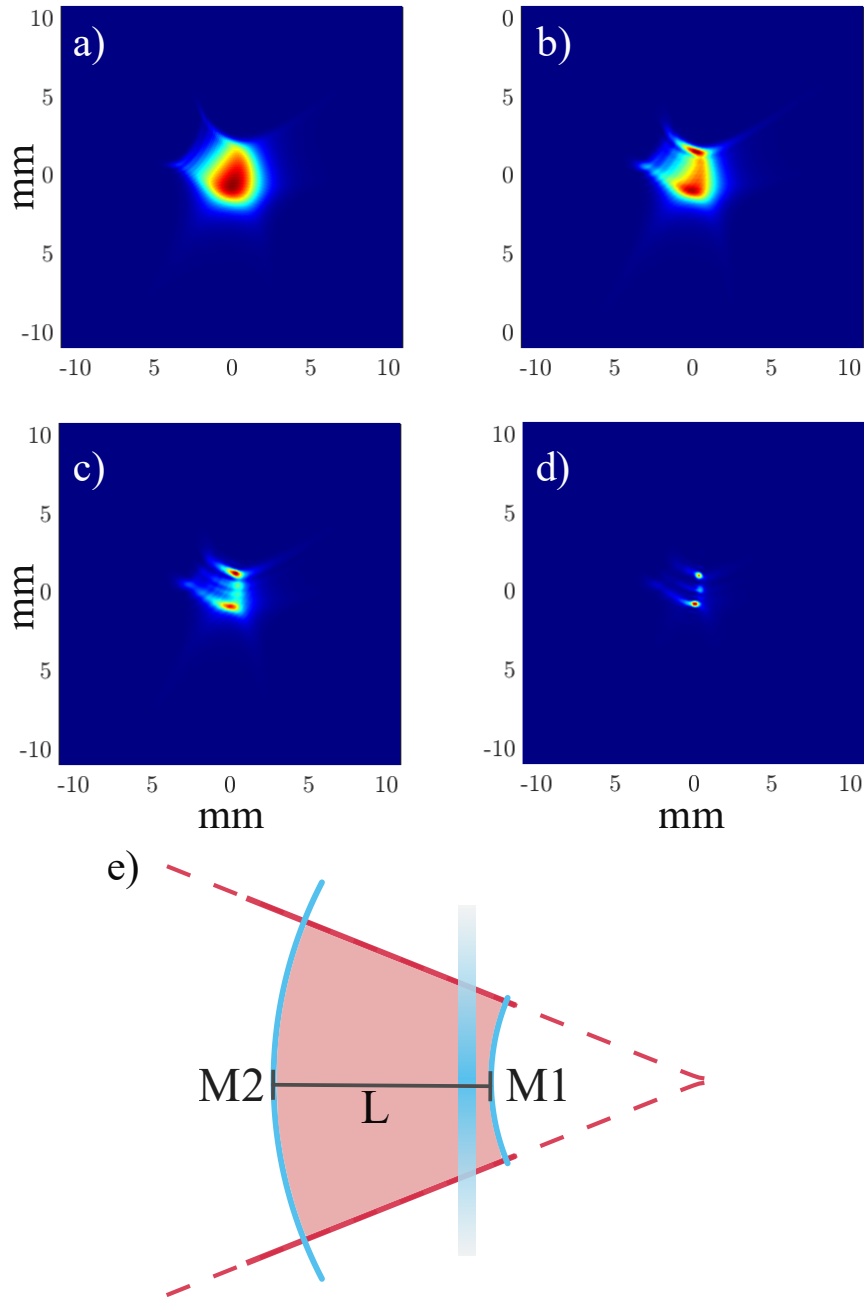


Figure 5.11: An aberrated beam with P/P_{cr} ratio of 1 850 in the input plane after propagating a round-trip in the cavity depicted in figure 5.3. a) (b,c,d) shows the 1st(2nd, 3rd, 4th) round trip. The shape is changed every round trip, as the beam is not perfectly mode matched to the cavity, because of the present aberrations altering the wave-front. There is clear indication of self focusing, and as the beam has formed 4(c) and 3(d) distinct structures of high intensity small scale self focusing also appears to be present.

the lab, but it is closer to the focus to keep the matrices somewhat reasonable. In the previous chapter the implemented cavity has its defocusing mirror at $z_1 = 80z_0$ and its focusing mirror at $z_2 = 160z_0$, while the simulated cavity has its defocusing mirror at $z_1 = 40z_0$ and focusing mirror at $z_2 = 80z_0$.

While being closer to the focus the simulated cell is also shorter. There has been

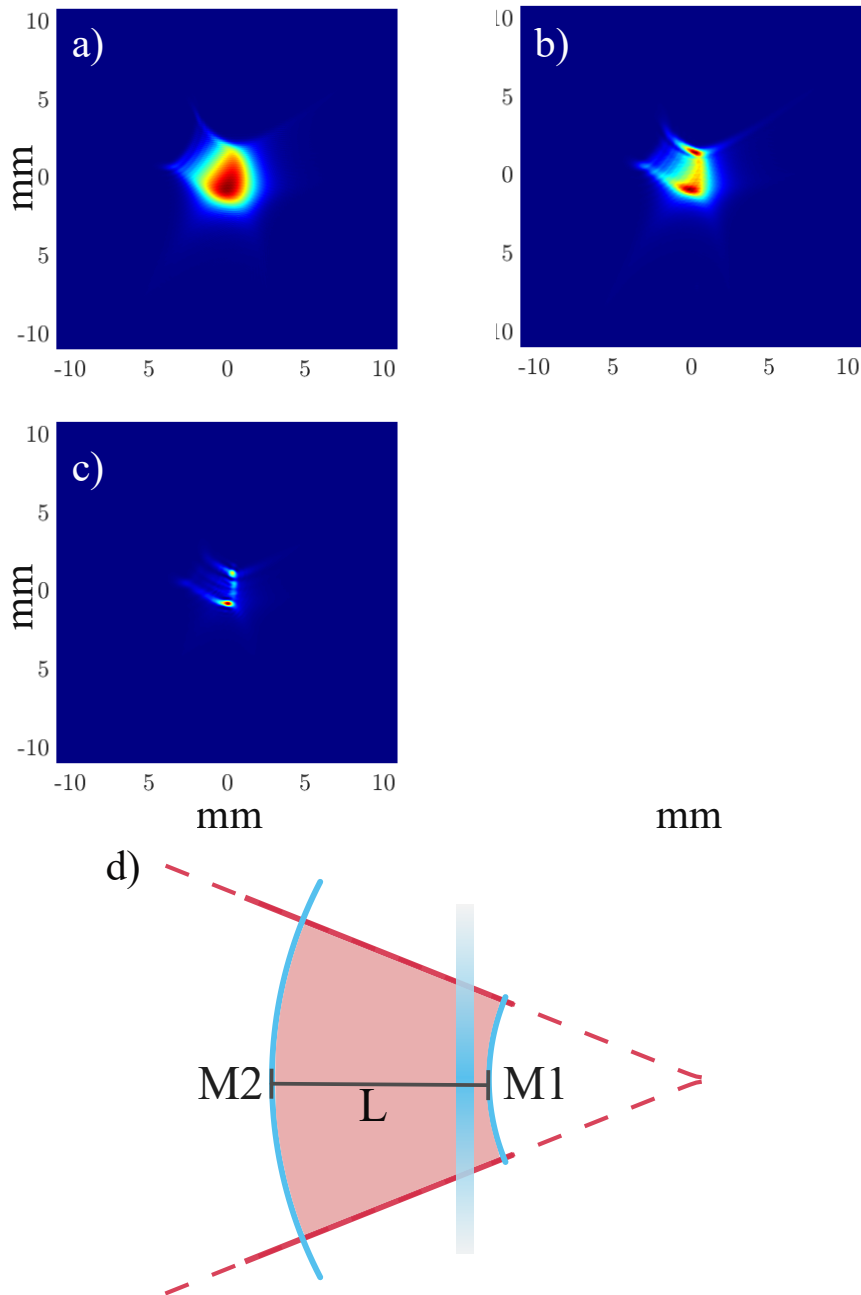


Figure 5.12: An aberrated beam with P/P_{cr} ratio of 3 300 in the input plane after propagating a round-trip in the cavity depicted in figure 5.3. a) (b,c,d) shows the 1st(2nd, 3rd, 4th) round trip. The shape is changed every round trip, as the beam is not perfectly mode matched to the cavity, because of the present aberrations altering the wave-front. The intensity is high, and the beam appears to enhance hot spots. The beam in c) is considered filamented and the fourth roundtrip was not simulated.

a recent article claiming that small scale self focusing may be suppressed as the beam propagates in free space due to different transverse k propagating at different angles [34]. The simulations are performed for a continuous beam, to only study the spatial evolution per round trip.

There are also a number of multi-plate solutions, where SPM in a bulk material

is obtained without an MPC but by instead using flat mirrors[35]. Such simulation was performed by taking the beam to the plane of the bulk material, where its phase was removed (which gave it a flat phase) perfectly collimating the beam. The beam was then propagated the same distances as in the simulated cell, but without the mirrors. This was performed for two powers, 200 and 1 850 times the critical power, and the result is shown in figures 5.13 and 5.14. In the lower power case, figure 5.13 the beam seems to mainly reshape, losing its original drop-like shape, while in the higher power case, figure 5.14 seems to keep the structure while self focusing more rapidly, possibly also with small scale self focusing.

While it is hard to draw conclusions based on a limited number of simulation, it indicates that the simulation code can be used to study the difference between Multi-plate geometries and different MPC's. The main difference between the simulated Multi-Plate geometry and MPC is that one beam has a flat phase and is reflected on planar surfaces, while the other is diverging(converging) and re-(de)focused at the mirror interfaces. In other MPC's there is also an accumulation of Gouy phase, which may affect the spatial beam.

The realistic beam is randomly generated, and for future reference it might be better to generate beams less randomly. This is possible, and would allow study of how specific aberrations affect the beam quality in an MPC. It would even be possible to generate a beam based on the output of a laser, to see how this specific profile would be affected.

A final notes is that there are additional effects that come into play, such as temporal effects that have not been included in this work [36–38]. There are also limitations on the model, as the chosen approach is scalar. In [39] a non-paraxial and vectorial approach is taken, enabling the model to handle the catastrophic collapse. There is however still problems related to those cases in the physical MPC's, and as this is something that in general should be avoided it might not be necessary. On the other hand it could provide additional insight in the self focusing dynamics of an MPC.

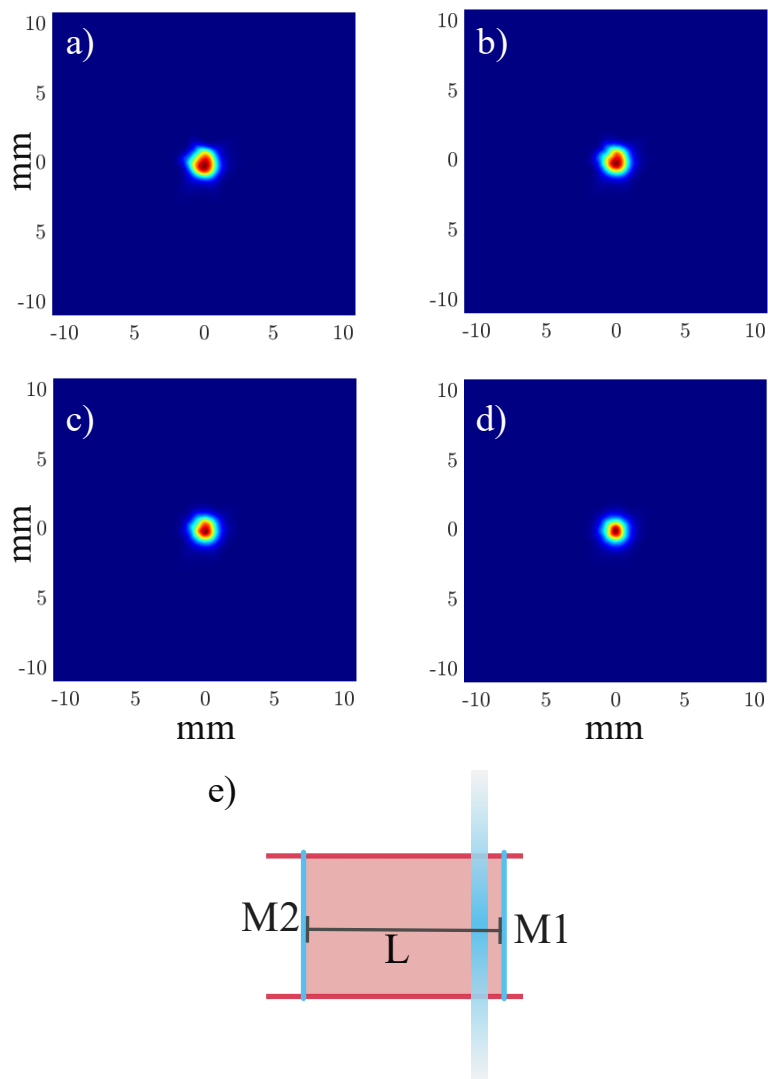


Figure 5.13: Aberrated beam of power $200P_{cr}$ propagated in a geometry as the one in figure 5.3 but collimated and with flat mirrors instead. Self focusing appears to alter the mode.

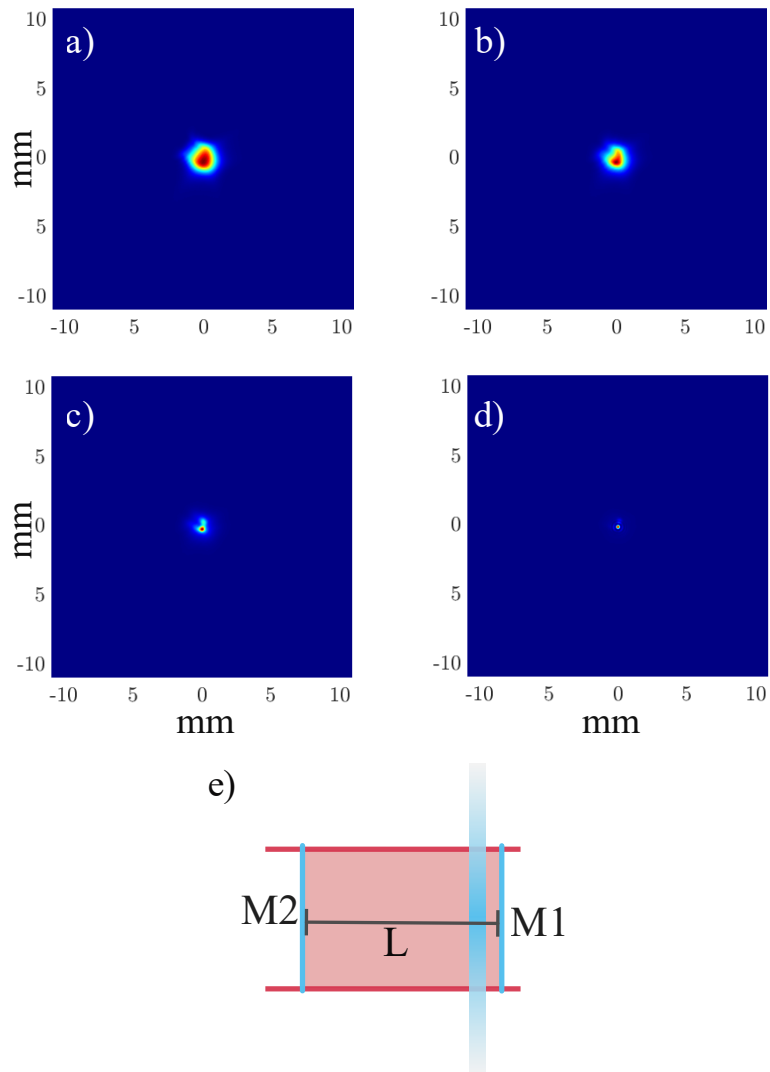


Figure 5.14: Aberrated beam of power $1.850P_{cr}$ propagated in a geometry as the one in figure 5.3 but collimated and with flat mirrors instead. Self focusing is apparent and even catastrophic.

Chapter 6

Conclusion and outlook

In this work a novel and compact convex-concave MPC not utilizing the Herriott configuration has been designed, implemented and characterized. The spectrum was broadened from 50 nm to 80 nm, and the pulses are compressed from 26 fs to 19 fs.

As the beam propagated in the implemented MPC it became very astigmatic. This is something that should be avoided, which could be done by using segmented mirrors to compensate each round trip. It also motivates the use of the Herriott configuration, as the circular pattern induces equal astigmatism in the vertical and horizontal plane, thus cancelling out. Further examination of the beam profile is necessary to understand how and if the cell in itself affects the mode in additional ways, and what effects arise because of self focusing.

The output pulses need to be further optimized, both spatially and temporally. At the moment there is clipping on the out coupling mirror due to the mirror geometry, and the compression of the pulses could still be improved. It has been prepared to perform a D-scan [40], to further characterize the temporal pulses. Additional effort to improve the output beam quality are needed to make the beam useable for experiments.

In parallel a simulation tool has been implemented and tested, and a cavity similar to the one implemented in the laboratory has been simulated for different peak powers. While the tool works rapidly for low intensities, when the nonlinear step can be made long, it becomes slow when a large number of steps are required, which is the case for high intensities requiring a short step. The computational speed also scales with the size of the beam matrices, that need fine grids to resolve the transverse k -domain and to not prematurely seed multiple filamentation. At the same time, the numerical window needs to be large enough for the beam not to touch the edges. If this happens the beam is reflected, refolded into itself. This is something that becomes important when cavities far away from the focus are simulated, as the window needs to be enlarged. Because of this, the matrices rapidly become large, which increases the computational cost due to a large number of Fourier transforms being required for large matrices. The computational cost might be reduced, as matrix multiplication can be performed using parallel computation and therefore might be sped up on a graphics card. In addition to speed there is also the question of memory, which further increases the computational cost.

The results for high power beams also indicate the need for nonlinear mode matching. Self focusing can be described as placing an additional lens in the cavity, which affects the curvature of the mode. If this effect is strong enough it needs to

be considered when designing the cell, which is implied by the results.

With the implemented simulation code, it will be possible to explore several parameters in MPC scaling. It would allow to study how different spatial beam profiles are affected in an MPC, comparing it to multi-plate solutions. It can also be explored how accumulated Gouy phase affect propagation in an MPC, and whether this plays a role in delaying large and/or small scale self focusing. This could provide important knowledge for further scaling of MPC's, as higher powers and shorter pulses are desired.

Bibliography

- [1] Jan Schulte et al. “Nonlinear pulse compression in a multi-pass cell”. In: *Opt. Lett.* 41.19 (Oct. 2016), pp. 4511–4514. DOI: 10.1364/OL.41.004511. URL: <https://opg.optica.org/ol/abstract.cfm?URI=ol-41-19-4511>.
- [2] Louis Daniault et al. “Single-stage few-cycle nonlinear compression of millijoule energy Ti:Sa femtosecond pulses in a multipass cell”. In: *Opt. Lett.* 46.20 (Oct. 2021), pp. 5264–5267. DOI: 10.1364/OL.442707. URL: <https://opg.optica.org/ol/abstract.cfm?URI=ol-46-20-5264>.
- [3] Alan Omar et al. *Spectral broadening of 2 mJ femtosecond pulses in a compact air-filled convex-concave multi-pass cell*. 2022. DOI: 10.1364/OL.481774. URL: <https://arxiv.org/abs/2211.14006>.
- [4] Kilian Fritsch et al. *Spectral broadening in convex-concave multipass cells*. 2022. DOI: 10.48550/ARXIV.2211.10241. URL: <https://arxiv.org/abs/2211.10241>.
- [5] B.E.A. Saleh and M.C. Teich. *Fundamentals of photonics*. 3rd ed. Wiley, 2019.
- [6] Max Born et al. *Principles of Optics: Electromagnetic Theory of Propagation, Interference and Diffraction of Light*. 7th ed. Cambridge University Press, 1999.
- [7] Robert W. Boyd. “Chapter 1 - The Nonlinear Optical Susceptibility”. In: *Nonlinear Optics (Third Edition)*. Ed. by Robert W. Boyd. Third Edition. Burlington: Academic Press, 2008, pp. 1–67. ISBN: 978-0-12-369470-6. DOI: <https://doi.org/10.1016/B978-0-12-369470-6.00001-0>. URL: <https://www.sciencedirect.com/science/article/pii/B9780123694706000010>.
- [8] J.W. Goodman. *Introduction to Fourier Optics*. McGraw-Hill physical and quantum electronics series. W. H. Freeman, 2005. ISBN: 9780974707723. URL: https://books.google.se/books?id=ow5xs%5C_Rtt9AC.
- [9] M. D. Feit and J. A. Fleck. “Beam nonparaxiality, filament formation, and beam breakup in the self-focusing of optical beams”. In: *J. Opt. Soc. Am. B* 5.3 (Mar. 1988), pp. 633–640. DOI: 10.1364/JOSAB.5.000633. URL: <https://opg.optica.org/josab/abstract.cfm?URI=josab-5-3-633>.
- [10] W. Nagourney. *Quantum Electronics for Atomic Physics*. Oxford Graduate Texts. OUP Oxford, 2010. ISBN: 9780199532629. URL: <https://books.google.se/books?id=EYRcn6ytA1IC>.
- [11] J.H. Marburger. “Self-focusing: Theory”. In: *Progress in Quantum Electronics* 4 (1975), pp. 35–110. ISSN: 0079-6727. DOI: [https://doi.org/10.1016/0079-6727\(75\)90003-8](https://doi.org/10.1016/0079-6727(75)90003-8). URL: <https://www.sciencedirect.com/science/article/pii/0079672775900038>.

- [12] A. Couairon and A. Mysyrowicz. “Femtosecond filamentation in transparent media”. In: *Physics Reports* 441.2 (2007), pp. 47–189. ISSN: 0370-1573. DOI: <https://doi.org/10.1016/j.physrep.2006.12.005>. URL: <https://www.sciencedirect.com/science/article/pii/S037015730700021X>.
- [13] P. L. Kelley. “Self-Focusing of Optical Beams”. In: *Phys. Rev. Lett.* 15 (26 Dec. 1965), pp. 1005–1008. DOI: 10.1103/PhysRevLett.15.1005. URL: <https://link.aps.org/doi/10.1103/PhysRevLett.15.1005>.
- [14] R. Y. Chiao, E. Garmire, and C. H. Townes. “Self-Trapping of Optical Beams”. In: *Phys. Rev. Lett.* 13 (15 Oct. 1964), pp. 479–482. DOI: 10.1103/PhysRevLett.13.479. URL: <https://link.aps.org/doi/10.1103/PhysRevLett.13.479>.
- [15] Gadi Fibich and Alexander L. Gaeta. “Critical power for self-focusing in bulk media and in hollow waveguides”. In: *Opt. Lett.* 25.5 (Mar. 2000), pp. 335–337. DOI: 10.1364/OL.25.000335. URL: <https://opg.optica.org/ol/abstract.cfm?URI=ol-25-5-335>.
- [16] E. L. DAWES and J. H. MARBURGER. “Computer Studies in Self-Focusing”. In: *Phys. Rev.* 179 (3 Mar. 1969), pp. 862–868. DOI: 10.1103/PhysRev.179.862. URL: <https://link.aps.org/doi/10.1103/PhysRev.179.862>.
- [17] Luat T. Vuong et al. “Collapse of Optical Vortices”. In: *Phys. Rev. Lett.* 96 (13 Apr. 2006), p. 133901. DOI: 10.1103/PhysRevLett.96.133901. URL: <https://link.aps.org/doi/10.1103/PhysRevLett.96.133901>.
- [18] Taylor D. Grow et al. “Collapse and Stability of Necklace Beams in Kerr Media”. In: *Phys. Rev. Lett.* 99 (13 Sept. 2007), p. 133902. DOI: 10.1103/PhysRevLett.99.133902. URL: <https://link.aps.org/doi/10.1103/PhysRevLett.99.133902>.
- [19] Anthony J. Campillo. “Small-Scale Self-focusing”. In: *Self-focusing: Past and Present: Fundamentals and Prospects*. Ed. by Robert W. Boyd, Svetlana G. Lukishova, and Y.R. Shen. New York, NY: Springer New York, 2009, pp. 157–173. ISBN: 978-0-387-34727-1. DOI: 10.1007/978-0-387-34727-1_6. URL: https://doi.org/10.1007/978-0-387-34727-1_6.
- [20] Marc Hanna et al. “Nonlinear temporal compression in multipass cells: theory”. In: *J. Opt. Soc. Am. B* 34.7 (July 2017), pp. 1340–1347. DOI: 10.1364/JOSAB.34.001340. URL: <https://opg.optica.org/josab/abstract.cfm?URI=josab-34-7-1340>.
- [21] D. Herriott, H. Kogelnik, and R. Kompfner. “Off-Axis Paths in Spherical Mirror Interferometers”. In: *Appl. Opt.* 3.4 (Apr. 1964), pp. 523–526. DOI: 10.1364/AO.3.000523. URL: <https://opg.optica.org/ao/abstract.cfm?URI=ao-3-4-523>.
- [22] Anne-Lise Viotti et al. “Multi-pass cells for post-compression of ultrashort laser pulses”. In: *Optica* 9.2 (Feb. 2022), pp. 197–216. DOI: 10.1364/OPTICA.449225. URL: <https://opg.optica.org/optica/abstract.cfm?URI=optica-9-2-197>.
- [23] Ann-Kathrin Raab et al. “Multi-gigawatt peak power post-compression in a bulk multi-pass cell at a high repetition rate”. In: *Opt. Lett.* 47.19 (Oct. 2022), pp. 5084–5087. DOI: 10.1364/OL.463960. URL: <https://opg.optica.org/ol/abstract.cfm?URI=ol-47-19-5084>.

- [24] Sizuo Luo et al. “Ultra-stable and versatile high-energy resolution setup for attosecond photoelectron spectroscopy”. In: (Jan. 2023). DOI: 10.48550/arXiv.2301.08919.
- [25] Thomas Oksenhendler et al. “High dynamic, high resolution and wide range single shot temporal pulse contrast measurement”. In: *Opt. Express* 25.11 (May 2017), pp. 12588–12600. DOI: 10.1364/OE.25.012588. URL: <https://opg.optica.org/oe/abstract.cfm?URI=oe-25-11-12588>.
- [26] Guoqiang Huang et al. “Generalizing the Gerchberg–Saxton algorithm for retrieving complex optical transmission matrices”. In: *Photon. Res.* 9.1 (Jan. 2021), pp. 34–42. DOI: 10.1364/PRJ.406010. URL: <https://opg.optica.org/prj/abstract.cfm?URI=prj-9-1-34>.
- [27] Rick Trebino and Daniel Kane. “Using phase retrieval to measure the intensity and phase of ultrashort pulses: Frequency-resolved optical gating”. In: *Journal of The Optical Society of America A-optics Image Science and Vision - J OPT SOC AM A-OPT IMAGE SCI* 10 (May 1993), pp. 1101–1111. DOI: 10.1364/JOSAA.10.001101.
- [28] G. Méchain et al. “Organizing Multiple Femtosecond Filaments in Air”. In: *Phys. Rev. Lett.* 93 (3 July 2004), p. 035003. DOI: 10.1103/PhysRevLett.93.035003. URL: <https://link.aps.org/doi/10.1103/PhysRevLett.93.035003>.
- [29] Johan Hult. “A Fourth-Order Runge–Kutta in the Interaction Picture Method for Simulating Supercontinuum Generation in Optical Fibers”. In: *Journal of Lightwave Technology* 25.12 (2007), pp. 3770–3775. DOI: 10.1109/JLT.2007.909373.
- [30] Marc Hanna et al. “Nonlinear beam matching to gas-filled multipass cells”. In: *OSA Continuum* 4.2 (Feb. 2021), pp. 732–738. DOI: 10.1364/OSAC.418247. URL: <https://opg.optica.org/osac/abstract.cfm?URI=osac-4-2-732>.
- [31] Marcus Seidel et al. “Factor 30 Pulse Compression by Hybrid Multipass Multiple Spectral Broadening”. In: *Ultrafast Science 2022* (Apr. 2022), pp. 1–10. DOI: 10.34133/2022/9754919.
- [32] Peter Dirksen et al. “Aberration retrieval using the extended Nijboer-Zernike approach”. In: *Journal of Microlithography, Microfabrication, and Microsystems* 2 (Jan. 2003). DOI: 10.1117/1.1531191.
- [33] Virendra N. Mahajan. “Zernike Polynomials and Optical Aberrations”. In: *Appl. Opt.* 34.34 (Dec. 1995), pp. 8060–8062. DOI: 10.1364/AO.34.008060. URL: <https://opg.optica.org/ao/abstract.cfm?URI=ao-34-34-8060>.
- [34] Mikhail Martyanov et al. “Suppressing small-scale self-focusing of high-power femtosecond pulses”. In: *High Power Laser Science and Engineering* 11 (2023), e28. DOI: 10.1017/hpl.2023.20.
- [35] Meenkyo Seo et al. “High-contrast, intense single-cycle pulses from an all thin-solid-plate setup”. In: *Opt. Lett.* 45.2 (Jan. 2020), pp. 367–370. DOI: 10.1364/OL.382592. URL: <https://opg.optica.org/ol/abstract.cfm?URI=ol-45-2-367>.

- [36] Scott A. Diddams et al. “Amplitude and phase measurements of femtosecond pulse splitting in nonlinear dispersive media”. In: *Opt. Lett.* 23.5 (Mar. 1998), pp. 379–381. DOI: 10.1364/OL.23.000379. URL: <https://opg.optica.org/ol/abstract.cfm?URI=ol-23-5-379>.
- [37] Alexander L. Gaeta. “Catastrophic Collapse of Ultrashort Pulses”. In: *Phys. Rev. Lett.* 84 (16 Apr. 2000), pp. 3582–3585. DOI: 10.1103/PhysRevLett.84.3582. URL: <https://link.aps.org/doi/10.1103/PhysRevLett.84.3582>.
- [38] P. Chernev and V. Petrov. “Self-focusing of light pulses in the presence of normal group-velocity dispersion”. In: *Opt. Lett.* 17.3 (Feb. 1992), pp. 172–174. DOI: 10.1364/OL.17.000172. URL: <https://opg.optica.org/ol/abstract.cfm?URI=ol-17-3-172>.
- [39] R. de la Fuente, O. Varela, and H. Michinel. “Fourier analysis of non-paraxial self-focusing”. In: *Optics Communications* 173.1 (2000), pp. 403–411. ISSN: 0030-4018. DOI: [https://doi.org/10.1016/S0030-4018\(99\)00637-9](https://doi.org/10.1016/S0030-4018(99)00637-9). URL: <https://www.sciencedirect.com/science/article/pii/S0030401899006379>.
- [40] Sytcevich, Ivan and Guo, Chen and Mikaelsson, Sara and Vogelsang, Jan and Viotti, Anne Lise and Alonso, Benjamin and Romero, Rosa and Guerreiro, Paulo T. and Sola, Ínigo J. and L’Huillier, Anne and Crespo, Helder and Miranda, Miguel and Arnold, Cord L. “Characterizing ultrashort laser pulses with second harmonic dispersion scans”. eng. In: *Journal of the Optical Society of America B: Optical Physics* 38.5 (2021), 1546–1555. ISSN: 0740-3224. DOI: {10.1364/JOSAB.412535}. URL: %7Bhttp://dx.doi.org/10.1364/JOSAB.412535%7D.